NASA TECHNICAL NOTE

NASA TN D-4443

LOCAL AFTERBODY HEAT TRANSFER TO A BLUNT TWO-DIMENSIONAL CONFIGURATION AT MACH 8

by Dennis M. Bushnell

Langley Research Center
Langley Station, Hampton, Va.

NATIONAL AERONAUTICS AND SPACE ADMINISTRATION • WASHINGTON, D. C. • JULY 1968

NASA TN D-4443

LOCAL AFTERBODY HEAT TRANSFER TO A BLUNT TWO-DIMENSIONAL CONFIGURATION AT MACH 8

By Dennis M. Bushnell

Langley Research Center
Langley Station, Hampton, Va.

NATIONAL AERONAUTICS AND SPACE ADMINISTRATION

For sale by the Clearinghouse for Federal Scientific and Technical Information
Springfield, Virginia 22151 – CFSTI price $3.00

LOCAL AFTERBODY HEAT TRANSFER TO A BLUNT TWO-DIMENSIONAL CONFIGURATION AT MACH 8*

By Dennis M. Bushnell
Langley Research Center

SUMMARY

Local heat-transfer rates and pressures were measured on a blunt two-dimensional configuration the afterbody of which was subjected to an extensive region of separated flow. The investigation was conducted at a free-stream Mach number of 8 and at free-stream Reynolds numbers based on the model face width of 2 inches (5.08 cm) from 1.27×10^5 to 7.55×10^5.

The predictions from two theories were compared with the heat-transfer data obtained in the afterbody region. One of these theories was a constant-pressure integral method utilizing profiles from similar solutions for enthalpy and velocity distributions. The other theory was a local flat-plate method in which the velocity and enthalpy conditions obtained from the integral method in the reverse-flow region were used as effective free-stream quantities. Both theories were in reasonable agreement with the general level of the data. The integral method predicted the correct trend in the vicinity of the separation point, whereas the flat-plate method gave the correct trend over the aft portion of the afterbody.

INTRODUCTION

The current use of atmospheric braking during the reentry of a space vehicle has necessitated the development of methods for predicting the severe heating which occurs during deceleration. For the forward portion of the vehicle, where the flow is attached and the heat transfer is the highest, theoretical predictions have been successful. However, for the aft portion of the vehicle, which is typically a region of separated flow, a satisfactory method of predicting local heating has not yet been developed. The flow separation which occurs over the aft portion of a vehicle is usually termed "free" separation, as opposed to the "forced" separation which is generally caused by deflected flaps or shock impingement.

*The information presented herein was offered as a thesis in partial fulfillment of the requirements for the degree of Master of Science in Mechanical Engineering, University of Virginia, Charlottesville, Virginia, June 1967.

Several approximate methods are currently available for predicting the local heat transfer in a "forced" laminar separated flow which reattaches on a surface. All of these methods employ some integral form of the boundary-layer equations. The first method appeared in reference 1, where the assumptions of polynomial profiles for the velocity and static enthalpy distributions, constant pressure, and zero boundary-layer thickness at the separation point were made. Primarily because of the latter assumption, the method is not applicable in the vicinity of the separation point.

The second method (ref. 2) is an approach similar to earlier work in references 3 and 4, except for the addition of the integral energy equation. This method employs the reverse-flow velocity and enthalpy profiles from the similar solutions in reference 5. It was successfully used in predicting local heat transfer in separated flows caused by deflected flaps and shock-wave boundary-layer interactions.

A third approach to the problem of predicting local heat transfer in a region of forced separation was presented in reference 6, where the Dorodnitsyn method of integral relations was employed. Although the method could be used to predict local heat transfer, no calculations or comparisons with experimental data were presented.

Because the second method (ref. 2) has thus far been successful in predicting local heat transfer for forced separation, it may be expected to provide good predictions for the free-separation problem. The purpose of the present investigation is to compare with experimental afterbody data the results of an approach similar to that of reference 2 as applied to afterbody flows, but simplified by the assumption of constant pressure (see appendix A for details of method). The data used for comparison were obtained at a Mach number of 8 on a two-dimensional blunt configuration which had an extensive region of separated flow at essentially constant pressure.

SYMBOLS

a	velocity profile parameter, $\frac{Y_{u=0}}{\delta}$
b	enthalpy profile parameter, ζ'_w
c_1, c_2, c_3 c_4, c_5, c_6	coefficients in polynomial curve fit of integral parameter (tables I and II)
c_p	specific heat at constant pressure
D	model face width, 2 inches (5.08 centimeters)

d_1, d_2, d_3
d_4, d_5, d_6 coefficients in polynomial curve fit of integral parameter (table III)

E integral parameter, $\int_0^{\delta} (\zeta - 1) f' dY$

f function related to stream function (eq. (23))

H stagnation enthalpy; $h + \frac{u^2}{2}$

h static enthalpy

$\overline{H}$ integral parameter, θ_i / δ_i^*

J integral parameter, θ_i^* / δ_i^*

k thermal conductivity

l distance along afterbody of model (see fig. 1(a))

M Mach number

N_{Pr} Prandtl number

P integral parameter, $\delta_i^* \left[\frac{\partial (U/U_e)}{\partial Y} \right]_w$

p pressure

Q integral parameter, $\delta_i^* \left[\frac{d}{dY} \left(\frac{S}{S_w} \right) \right]_w$

q heat-transfer rate

$R_{\infty,D}$ free-stream Reynolds number based on model face width

$\overline{R}$ integral parameter, $2\delta_i^* \int_0^{\delta} \left[\frac{\partial (U/U_e)}{\partial Y} \right]^2 dY$

$S = \zeta - 1$

s skin thickness

T temperature

$t = \dfrac{T}{T_{s,e}}$

$\overline{T}$ integral parameter, $\dfrac{E}{\delta_i^*(t_w - 1)}$

u,v velocities in x- and y-directions

U,V velocities in transformed coordinate system (eq. (8))

x,y longitudinal and normal coordinates

X,Y transformed longitudinal and normal coordinates (eq. (5))

$\tilde{X}$ distance defined in equation (15)

$\beta = \dfrac{2}{u_e^2}\dfrac{du_e}{dx}\dfrac{1}{t_e\rho_w\mu_w}\displaystyle\int_0^x \rho_w\mu_w u_e\, dx$

δ boundary-layer thickness (where $f' = 0.9995$)

$\delta_i^* = \displaystyle\int_0^\delta \left(1 - \frac{U}{U_e}\right)dY$

$\tilde{\delta}_i^* = \dfrac{\delta_i^*}{(\delta_i^*)_o}$

$\zeta = \dfrac{H_s}{H_{s,e}}$

η similarity variable (eq. (24))

θ angle defined in figure 1(a)

$\theta_i = \displaystyle\int_0^\delta \frac{U}{U_e}\left(1 - \frac{U}{U_e}\right)dY$

$\theta_i^* = \displaystyle\int_0^\delta \frac{U}{U_e}\left[1 - \left(\frac{U}{U_e}\right)^2\right]dY$

λ parameter defined in equation (6)

μ dynamic viscosity

ν kinematic viscosity

ρ density

τ time

$\phi = \frac{\rho\mu}{\rho_w \mu_w}$

ψ stream function (eq. (7))

Subscripts:

e local flow quantity external to boundary layer

o separation point

rev conditions at maximum velocity in reverse-flow region

s local stagnation conditions

t stagnation conditions behind a normal shock at free-stream conditions

w wall conditions

∞ free-stream conditions

* value at dividing streamline

Single, double, and triple primes denote first, second, and third derivatives with respect to η. $\left(\text{Note that, in addition, } f' = \frac{U}{U_e} = \frac{u}{u_e}.\right)$

APPARATUS

Tunnel

The model tests were conducted in the Langley Mach 8 variable-density hypersonic tunnel. This tunnel has an axially symmetric nozzle with contoured walls. The test medium is air. The average test-section Mach number variation with stagnation pressure is given in reference 7. For the present investigation the stagnation pressure was varied from 130 to 1055 psia (0.896 to 7.27 MN/m^2). The corresponding Mach number range is from 7.74 to 7.95. The range of free-stream Reynolds numbers based on the 2-inch (5.08-cm) model face width was from 1.27×10^5 to 7.55×10^5. Nominal stagnation temperature was 900° F (755° K). Further details concerning the facility are available in reference 8.

Model

General description.- A sketch of the model is shown in figure 1(a). The configuration is basically a section of a cylinder which was mounted normal to the free-stream flow direction with the blunt face forward at zero angle of attack. The supporting struts attached to the ends of the model did not extend above the model center line so that schlieren photographs of the afterbody flow could be taken. The model was constructed with a thin skin silver-soldered to internal supports. Type 347 stainless steel was used, and the model had a large ratio of span to face width (4.5) in order to minimize end effects. The nominal skin thickness was 0.030 inch (0.076 cm). Photographs showing front and oblique views of the model are presented in figure 1(b).

Instrumentation.- Figure 1(a) also shows the location of the pressure orifices and thermocouples. Pressure orifices were installed on the model at the indicated positions with the use of monel tubing having an inside diameter of 0.040 inch (0.102 cm); the tubing was mounted flush with, and normal to, the local surface. The afterbody of the model was also instrumented with thermocouples made from No. 30 chromel-alumel wire 0.010 inch (0.025 cm) in diameter. The thermocouples were installed in the positions shown by drilling two 0.011-inch-diameter (0.0279-cm-diameter) holes 0.020 inch (0.0508 cm) apart, inserting the individual thermocouple wires into these holes, silver soldering the wires in place, and fairing the surface flush.

Equipment

The temperature-time history of the model was recorded on magnetic tape with an analog-to-digital data recording system at a rate of 40 samples per second. Each pressure orifice on the face was connected to two strain-gage pressure transducers – one with a range from 0 to 1 psia (0 to 6.89×10^3 N/m^2) and the other with a range from 0 to 10 psia (0 to 6.89×10^4 N/m^2). The orifices on the afterbody were connected to thermocouple vacuum gages with a nominal range from 0.01 psia (6.89×10 N/m^2) to 0.3 psia (2.07×10^3 N/m^2). The output from these pressure-measuring devices was also recorded by the analog-to-digital data recorder at 40 samples per second. Tunnel stagnation pressure was measured with a Bourdon tube gage.

TEST PROCEDURES AND DATA REDUCTION

Heat-Transfer Data

The heat-transfer data were obtained by the transient heating technique. For this technique, steady flow was established in the test section with the model retracted from the flow; the model was then injected into the test section, the total injection time being approximately 0.2 second. Data were taken for approximately 8 seconds, after which

the model was removed from the airflow and brought to isothermal conditions at approximately room temperature (90° F (305° K)) in preparation for another test.

The temperature data were reduced to heating rates by use of the calorimeter equation

$$q = \rho c_p s \frac{dT}{d\tau} \tag{1}$$

wherein both conduction and radiation heat transfer are neglected. The radiation heat transfer was measured by inserting the model into the tunnel test section with no airflow and monitoring the skin-temperature variation with time. From such tests the radiation heat transfer to the model from the test-section walls was determined to be approximately 0.5 percent of the lowest aerodynamic heating rate measured and was therefore negligible.

For test times of less than 1 second, when the model was essentially isothermal, the maximum heat transfer by conduction along the skin at the thermocouple locations was calculated to be approximately 8 percent of the lowest aerodynamic heating rate measured. As this conduction error was generally smaller than other experimental errors, a conduction correction was not applied during the data reduction and equation (1) was used to calculate the aerodynamic heating. The local skin thickness was measured for each thermocouple position. The values of ρ and c_p used were 500.5 lbm/ft^3 (8×10^3 kg/m^3) and 0.12 Btu/lbm-°R (502 joules/kg-°K), respectively (ref. 9). In addition to conduction effects there are possible errors in measured temperatures, skin thickness, and the values of density and specific heat of the skin; hence, the final values of heating rate are considered accurate to within 15 percent.

Pressure Data

The pressure data were obtained during the same runs as the heat-transfer data. The run time of 8 seconds was sufficient to allow the gages to reach a steady-state condition. As the measured wall temperature on the afterbody did not change more than 20° R (11.1° K) during this interval, the pressure and heat-transfer data were obtained at essentially the same value of wall temperature. The pressure sensors were calibrated before the tests and checked during the testing period. The transducers that were used to measure the pressure over the face of the model are accurate to within 1 percent of the full-scale reading. Therefore, the maximum error in the face-pressure data is 5 percent. The thermocouple vacuum gages used for the afterbody pressure readings are accurate to within 0.5 percent of the full-scale reading. However, because of the low pressures on the afterbody and the difficulty of calibration in this range, the final data are accurate only to within 10 percent. Schlieren photographs were obtained during the same tests as the heat-transfer and pressure data.

RESULTS AND DISCUSSION

Flow Field

Shown in figure 2 are schlieren photographs of the flow field over the model for several values of free-stream Reynolds number. The dark area in the vicinity of the model corner indicates an expansion region. The light area immediately beneath this expansion region indicates a compression region, and therefore the upstream flow was apparently overexpanded. (The expansion and compression regions under discussion are labeled in fig. 3(a).) To ascertain if the overexpansion was large enough to cause the flow to attach to the afterbody, this section of the model was coated with oil and then injected into the airstream. For a small distance just downstream of the corner, the oil was removed by the airstream (see fig. 3(b)), an indication that the flow does remain attached for this distance along the afterbody. The fact that the oil was undisturbed on the remainder of the afterbody indicated the presence of a low-shear region of separated flow. The attachment of the flow for some small distance downstream of the corner is in agreement with results reported in reference 10 for flow separation from a flat-based cone-cylinder configuration.

The dark band which appears underneath the compression region on the photographs in figures 2 and 3(a) at an angle to the afterbody represents a region of decreasing density as the body is approached (inasmuch as the schlieren method gives density gradient). Since the pressure is nearly constant in this region, this decreasing density corresponds to an increase in temperature as the flow velocity is reduced. The largest temperature gradient generally occurs in the outer portion of the viscous mixing region, which grows after flow separation occurs; hence, the dark band corresponds to this portion of the flow region. The inclination of this dark band with respect to the free-stream flow direction becomes greater with increasing Reynolds number, an indication that the ratio of the afterbody pressure to free-stream pressure should decrease with increasing Reynolds number. For the purpose of calculating afterbody pressure, the slope of the dark band under discussion was assumed to be equal to the local flow angle at the edge of the viscous region. The location at which this slope was measured is shown in figure 3(a). On some of the photographs in figure 2 (ones for the higher values of $R_{\infty,D}$), the neck of the wake and the beginning of the far wake are visible.

Pressure Distributions

Face.- Figure 4 shows the measured pressure distribution over the model face for the range of free-stream Reynolds numbers of this investigation. As expected, the distribution over the face is essentially independent of Reynolds number. Also shown in figure 4 is a modified Newtonian distribution. The surface pressure falls below the

Newtonian value as θ increases, as previously noted for sections of spheres (see ref. 11). In the heat-transfer theory summarized in appendix A, the quantity $\int p_e u_e \, dx$ is required, with the integral evaluated from the stagnation point to the separation point. To evaluate this quantity over the model face, the dashed line shown faired through the data in figure 4 was used. This curve was faired into the sonic pressure ratio at the corner (0.528).

Afterbody.- Figures 5(a) to 5(c) illustrate typical measured afterbody pressure distributions. The figures also show the level obtained by assuming an isentropic expansion from the stagnation point to the afterbody flow angle measured in accordance with the method described in the flow-field discussion. For this calculation, the flow angle for the Mach 1 condition was assumed to be equal to the flow angle behind an oblique shock which just gives a Mach number of 1 downstream of the shock at the free-stream conditions. This angle is approximately 43.6° and was obtained from the tables of reference 12. (The Mach 1 inclination near the surface of the model would be greater, as indicated by the data in figure 4.) The flow was then assumed to undergo a Prandtl-Meyer expansion from 43.6° to the final flow angle measured on the afterbody from schlieren photographs like those of figure 2. As discussed previously, this flow angle was taken as the slope of the dark band at the point indicated in figure 3(a). In order to calculate the afterbody pressure by the method described, it was necessary to assume that the recompression of the afterbody flow discussed in the flow-field section was isentropic.

The other pressure level shown in figure 5 was calculated by using the method of reference 13. The value of u_*/u_e used in the calculation was 0.587 which is the value given by the similar solution in reference 14 for an external stream mixing with an infinite quiescent reservoir. In reference 3 it is shown that this value will usually be achieved only far downstream in an actual laminar mixing region and that for low values of Reynolds number this value may never be reached in the near wake. Therefore the value of u_*/u_e of 0.587 and the method of reference 13 should give a value of afterbody pressure which would be approached asymptotically as the Reynolds number is increased (with the assumption that the afterbody flow remained laminar). This phenomenon is discussed in more detail in reference 15.

In figure 5 the data indicate that the afterbody pressure is essentially constant. Also, the general level of the experimental data is in reasonable agreement with the level calculated by using the measured afterbody flow angle. In figure 5(a), which is for a low Reynolds number, the level calculated by the method of reference 13 is considerably below that of the data; however, as expected, the data at higher values of $R_{\infty,D}$ are in closer agreement with this calculated level (see figs. 5(b) and 5(c)).

To show the variation of afterbody pressure with Reynolds number, the pressure at three values of l/D has been plotted as a function of Reynolds number in figure 6. From this figure it is evident that as the Reynolds number is increased up to about 4×10^5, the afterbody pressure ratio tends to approach the value predicted by the method of reference 13. For $R_{\infty,D} > 4 \times 10^5$ the pressure ratio drops below the value predicted by this method. This latter result may be caused by transition to turbulent flow in the near wake. The near-wake transition studies for axisymmetric blunt bodies reported in reference 16 (wherein a model cross section somewhat similar to the one used in the present investigation was employed) indicate that 4×10^5 would be a reasonable Reynolds number at which to expect transition in the near wake.

Heat-Transfer Distributions

Variation along afterbody.- The measured afterbody heat-transfer distributions are presented in figure 7, each part of which represents a different value of test Reynolds number. Also shown in the figure is the distribution calculated by using the method given in appendix A and the measured pressure level. The method (appendix A) is essentially that of reference 2 except that it is simplified for application to the afterbody problem by the assumption of constant pressure. The integral constant-pressure boundary-layer equations are solved by using the reverse-flow profiles of reference 5, which are uncoupled from the pressure-gradient parameter. The pressure level used in the calculation is noted in each figure.

The value of t_w for the actual data varied from 0.386 to 0.44. Inasmuch as the theoretical calculations were carried out for a value of t_w (wall- to total-temperature ratio $T_w/T_{s,e}$) of 0.35 to obtain the distribution shown in figure 7, it was assumed that the variation of $\zeta'_w/\left(\zeta'_w\right)_{\tilde{X}=0}$ with $\tilde{X}$ (fig. 8) was independent of t_w over the interval from 0.35 to 0.44. The value of $\left(\zeta'_w\right)_{\tilde{X}=0}$ for the t_w value pertinent to the test under consideration was used to obtain ζ'_w as a function of $\tilde{X}$. The pertinent value of t_w is given in each part of figure 7.

As shown in figure 7(a), the theory of appendix A indicates a large decrease in heat-transfer rate near the separation point, followed by a more gradual decrease along the rest of the afterbody. The data tend to agree with the prediction of the initial decrease, but as l increases the data show a trend of increased heating.

The distribution of the data appears reasonable if the physical flow picture is considered. The flow adjacent to the afterbody surface is a region of reverse flow. This flow might be expected to cause a sublayer (roughly equivalent to a flat-plate boundary layer) to form along the body. This equivalent flat-plate boundary layer would start at the rear of the body and grow in the negative l direction. Therefore, the heat-transfer rate might be expected to decrease as l decreases. The theory of appendix A

apparently fails to give the proper heat-transfer-rate distribution because this boundary condition at the rear of the model cannot be included in the theory.

This analogy between the sublayer near the afterbody surface and a flat-plate boundary layer can be utilized to calculate the afterbody heat-transfer rate by an approximate method that may be more realistic away from the separation point than is the method of appendix A. Basically, the inner (reverse-flow) portion of the velocity and enthalpy profiles is assumed to constitute an effective free-stream flow, which causes a flat-plate boundary layer to begin growing in the negative l-direction at the rear of the model afterbody. The nominal values of f' and ζ that characterize this flow were taken from the profiles obtained in the vicinity of the rear of the model by the method of appendix A. These values were $f'_{rev} = -0.05$ and $\zeta_{rev} = 0.5$ and are characteristic of the fairly flat maximum-velocity portion of the reverse-flow region. The value of ζ'_w as computed from the results of reference 17 for $\beta = 0$ (flat-plate) attached flow is 0.305. With this information and the local measured pressure level, a flat-plate heat-transfer-rate distribution was calculated by the method of reference 17 and is shown in figure 7 as the dashed lines. (The rear of the model was taken as the origin of the flat-plate flow.) In all parts of figure 7, flat-plate theory seems to predict the distribution away from the separation point, except in the immediate vicinity of the rear of the model.

In summary, the theory of appendix A correctly predicts the approximate level and the measured trend in heating near the separation point but not over the rest of the afterbody. The flat-plate theory predicts essentially the correct type of distribution over the rest of the afterbody, but the predicted level of heating does not increase as much with Reynolds number as the data.

After the present investigation had been completed, an approach to the prediction of afterbody heat transfer that was similar to the flat-plate method used herein appeared in reference 18. The approach was to solve the "free-shear-layer" problem and then apply the blunt-body attached-flow heat-transfer expression to the afterbody with the average separated-region quantities as effective external conditions. Base heating to a flat-based ogive-cylinder was successfully predicted by using this method. These results, together with those of the present investigation, indicate that the use of attached-flow expressions with local recirculating or reverse-flow quantities as effective external conditions appears to be a valid approach to the prediction of afterbody heat transfer in regions of separated flow.

Variation with Reynolds number.- In order to show a comparison between the experimental variation of heat transfer with Reynolds number and the variation predicted by the flat-plate theory, the heat-transfer rate at $l/D = 0.47$ is plotted as a function of the local unit Reynolds number $(\rho_e u_e/\mu_e)$ in figure 9. It is apparent that the increase in heat-transfer rate with unit Reynolds number for $\rho_e u_e/\mu_e > 1.5 \times 10^5$ per foot

(4.92×10^5 per meter) is greater for the data than for the theory. This increase with unit Reynolds number is probably associated with transition to turbulent flow in the near wake, as the value of unit Reynolds number where the increase occurs corresponds to $R_{\infty,D} = 4 \times 10^5$, which is the "transition Reynolds number" indicated by the pressure data of figure 6. (See discussion of fig. 6.)

Engineering estimates of afterbody heat transfer.- By using the flat-plate method, it may be possible to obtain approximate engineering estimates for heating in a region of separated afterbody flow without solving the equations of appendix A to obtain values for f'_{rev} and ζ_{rev}. To indicate a method by which these estimates might be obtained, figure 10 shows the quantities f'_{rev} and ζ_{rev} from reverse-flow similar solutions for $N_{Pr=1}$ and $\phi = 1$ plotted as functions of the velocity and enthalpy profile parameters at several values of t_w.

Figure 10(a), in which the values of ζ_{rev} have been normalized by using the appropriate value of t_w, shows that the normalization procedure partially collapses the curves for different values of t_w, but overemphasizes the variation of ζ_{rev} with b for a given t_w. Nevertheless, the fact that the curves are fairly flat and tend to group about a value of $\frac{\zeta_{rev} - \zeta_w}{1 - \zeta_w}$ of 0.2 indicates that this value would provide a reasonable estimate for the reverse-flow enthalpy parameter over a wide range of values of b and t_w; therefore, a solution for b by the method of appendix A may not be critical to obtain a reasonable estimate for ζ_{rev}.

The values of f'_{rev} shown in figure 10(b) exhibit a large variation with the parameter a. Therefore, a local estimate for a is needed in order to apply the flat-plate method. For large values of a (thick separated regions), an upper heating limit could be provided by using values for f'_{rev} ranging from -0.09 to -0.12 depending on the value of t_w.

For smaller values of a (less than 0.4) and in the absence of a solution to the equations of appendix A, an estimate for a can be made by extrapolating the initial slope of a with $\tilde{X}$. This initial slope can be obtained by solving equations (16) and (19) of appendix A for $da/d\tilde{X}$. Note that $d\bar{H}/d\tilde{X} = (d\bar{H}/da)(da/d\tilde{X})$ and, for example, at $\tilde{X} = 0$ (as the initial a slope is being ascertained) $P = 0$, $\tilde{\delta}_i^* = 1$, and $a = 0$. The result is

$$\left(\frac{da}{d\tilde{X}}\right)_{a=0} = \left(\frac{\bar{R}}{-\frac{J}{\bar{H}}\frac{d\bar{H}}{da} + \frac{dJ}{da}}\right)_{a=0}$$

The values of the integral parameters can be obtained from the coefficients in table I for $t_w = 0.35$ and from reference 4 for $t_w = 1$ and $t_w = 0.2$. The extrapolation of the initial slope gave a value for a near the rear of the model about 50 percent lower than the actual value computed by the method of appendix A; the heating would

therefore be underestimated by about 60 percent, as compared with the results obtained when using the method of appendix A. Thus, this extrapolation method is fairly crude and should be used only if rough estimates are desired.

Another possible method for estimating a value of a with which to enter figure 10(b) is to use an estimate of the physical distance to the dividing streamline. The procedure would be to obtain an afterbody flow angle (assumed constant) from correlations or knowledge of the afterbody pressure. The distance from the body surface to the local flow line drawn from the separation point parallel to the afterbody flow direction would then provide a rough estimate of the physical distance to the dividing streamline. From equation (24)

$$\int_0^{\eta_*} \frac{\rho_e}{\rho}\, d\eta = \frac{u_e \rho_e y_*}{\sqrt{2 \int_0^x \rho_w \mu_w u_e\, dx}}$$

When the information on the right-hand side of this equation is known, a value of $\int_0^{\eta_*} \frac{\rho_e}{\rho}\, d\eta$ with which to enter the reverse-flow velocity profiles can be obtained. The integral over x should be taken from the stagnation point. The value of a associated with the profile having the known value of $\int_0^{\eta_*} \frac{\rho_e}{\rho}\, d\eta$ is then an approximation of the local value of a.

In general, for a perfect gas

$$\int_0^{\eta_*} \frac{\rho_e}{\rho}\, d\eta = \frac{H_{s,e}}{h_e}\left[\int_0^{\eta_*} \zeta\, d\eta - \int_0^{\eta_*} (f')^2 d\eta \left(\frac{u_e^2}{2H_{s,e}}\right)\right]$$

The integrals $\int_0^{\eta_*} \zeta\, d\eta$ and $\int_0^{\eta_*} (f')^2 d\eta$ are given in figure 11 as functions of a. An approximate 20 percent overestimation of the local a near the rear of the model results when this iterative method is applied to the present data by using a value of y_* (distance to the dark band) obtained from the schlieren photographs of figure 2. Compared with results obtained when using the method of appendix A, the heating would be overestimated by about 15 percent. Therefore, this method appears to give better results than the previously discussed procedure of extrapolating the initial slope.

CONCLUSIONS

Local heat-transfer rates and pressures have been measured over the afterbody of a blunt two-dimensional configuration at a Mach number of 8. The afterbody of the model was subjected to an extensive region of separated flow. The model was tested at a

nominal value of wall- to total-temperature ratio of 0.4 and at free-stream Reynolds numbers based on face width from 1.27×10^5 to 7.55×10^5. The heat-transfer data were compared with the results of a constant-pressure integral method employing reverse-flow profiles and with the results of a flat-plate method. The following conclusions can be made:

1. The flow remains attached over the afterbody downstream of the corner of the model for a small distance before separation occurs.

2. The pressure level is essentially constant over the afterbody and decreases with increasing Reynolds number.

3. The measured heat-transfer rate decreases just downstream of separation and then increases in the downstream direction as the rear of the model is approached. The integral method correctly predicts the initial large decrease in heating, but also predicts a gradual decrease in heating toward the rear of the model, a trend opposite to that indicated by the data.

4. Away from the separation point, the flat-plate method predicts the correct type of heat-transfer-rate distribution for the lower Reynolds number data.

5. The deviation from the theoretical laminar predictions of both the heat-transfer and pressure data at the higher Reynolds numbers probably results from afterbody-flow transition beginning at a free-stream Reynolds number based on face width of about 4×10^5.

Langley Research Center,
National Aeronautics and Space Administration,
Langley Station, Hampton, Va., November 16, 1967,
129-01-08-38-23.

APPENDIX A

DETERMINATION OF LOCAL LAMINAR HEAT-TRANSFER DISTRIBUTION IN A CONSTANT-PRESSURE SEPARATED FLOW

As in the analysis of reference 2, the starting point of the method is the boundary-layer equations for a compressible perfect fluid. For the case of no streamwise pressure gradient, these equations are as follows:

Continuity:

$$\frac{\partial}{\partial x}(\rho u) + \frac{\partial}{\partial y}(\rho v) = 0 \tag{2}$$

Momentum:

$$\rho u \frac{\partial u}{\partial x} + \rho v \frac{\partial u}{\partial y} = \frac{\partial}{\partial y}\left(\mu \frac{\partial u}{\partial y}\right) \tag{3}$$

Energy:

$$\rho u \frac{\partial h}{\partial x} + \rho v \frac{\partial h}{\partial y} = \mu\left(\frac{\partial u}{\partial y}\right)^2 + \frac{\partial}{\partial y}\left(\frac{\mu}{N_{Pr}} \frac{\partial h}{\partial y}\right) \tag{4}$$

The introduction of a modified Lees transformation

$$\left.\begin{aligned} X &= \int_0^x \lambda \frac{p_e u_e}{p_\infty u_\infty} dx \\ Y &= \frac{u_e}{u_\infty} \int_0^y \frac{\rho}{\rho_\infty} dy \end{aligned}\right\} \tag{5}$$

where

$$\frac{\mu}{\mu_\infty} = \lambda \frac{T}{T_\infty} \tag{6}$$

and definition of a stream function ψ

$$\left.\begin{aligned} \frac{\partial \psi}{\partial y} &= \frac{\rho u}{\rho_\infty} \\ \frac{\partial \psi}{\partial x} &= -\frac{\rho v}{\rho_\infty} \end{aligned}\right\} \tag{7}$$

so that

$$\left.\begin{aligned} U &= \frac{\partial \psi}{\partial Y} \\ V &= -\frac{\partial \psi}{\partial X} \end{aligned}\right\} \tag{8}$$

transform equations (2) to (4) to the following analogs of the incompressible form of the boundary-layer equations:

Continuity:

$$\frac{\partial U}{\partial X} + \frac{\partial V}{\partial Y} = 0 \tag{9}$$

Momentum:

$$U \frac{\partial U}{\partial X} + V \frac{\partial U}{\partial Y} = \nu_\infty \frac{\partial^2 U}{\partial Y^2} \tag{10}$$

Energy:

$$U \frac{\partial S}{\partial X} + V \frac{\partial S}{\partial Y} = \nu_\infty \frac{\partial^2 S}{\partial Y^2} \tag{11}$$

These equations apply for a perfect gas with constant specific heats and a constant Prandtl number of 1 where

$$S = \frac{H_S}{H_{S,e}} - 1 = \zeta - 1$$

Integration of equation (10) across the boundary layer and the use of equation (9) give

$$\frac{d\theta_i}{dX} = \frac{\nu_\infty}{U_e^2} \left(\frac{\partial U}{\partial Y}\right)_w \tag{12}$$

Multiplication and division by δ_i^* give

$$\frac{d\left(\overline{H}\delta_i^*\right)}{dX} = \frac{\nu_\infty}{U_e \delta_i^*} P \tag{13}$$

where

$$\overline{H} = \frac{\theta_i}{\delta_i^*}$$

and

$$P = \delta_i^* \left[\frac{\partial\left(U/U_e\right)}{\partial Y}\right]_w$$

From the definitions

$$\frac{\delta_i^*}{\left(\delta_i^*\right)_o} = \tilde{\delta}_i^* \tag{14}$$

and

$$\tilde{X} = \frac{X \nu_\infty}{\left[\left(\delta_i^*\right)_o\right]^2 U_e} \tag{15}$$

the final form of the momentum equation can be written as

$$\frac{\overline{H}}{2}\frac{d\left(\tilde{\delta}_i^*\right)^2}{d\tilde{X}} + \left(\tilde{\delta}_i^*\right)^2\frac{d\overline{H}}{d\tilde{X}} = P \tag{16}$$

Multiplication of equation (10) by U and integration across the boundary layer together with the use of equation (9) result in

$$\frac{d\theta_i^*}{dX} = \frac{2\nu_\infty}{U_e^3}\int_0^\delta\left(\frac{\partial U}{\partial Y}\right)^2 dY \tag{17}$$

Again multiplication and division by δ_i^* give

$$\frac{d}{dX}\left(J\delta_i^*\right) = \frac{\nu_\infty}{U_e\delta_i^*}\overline{R} \tag{18}$$

where

$$J = \frac{\theta_i^*}{\delta_i^*}$$

and

$$\overline{R} = \frac{2\delta_i^*}{U_e^2}\int_0^\delta\left(\frac{\partial U}{\partial Y}\right)^2 dY$$

Then by the use of equations (14) and (15) the moment of momentum equation is written as

$$\frac{J}{2}\frac{d\left(\tilde{\delta}_i^*\right)^2}{d\tilde{X}} + \left(\tilde{\delta}_i^*\right)^2\frac{dJ}{d\tilde{X}} = \overline{R} \tag{19}$$

Integration of equation (11) across the boundary layer and the use of equation (9) give

$$\frac{dE}{dX} = -\frac{\nu_\infty}{U_e}\left[\frac{d\left(S/S_w\right)}{dY}\right]_w S_w \tag{20}$$

Multiplication and division by δ_i^* give

$$\frac{d\left(\overline{T}\delta_i^*\right)}{dX} = -\frac{\nu_\infty}{U_e\delta_i^*}Q\left(S_w\right) \tag{21}$$

where

$$\overline{T} = \frac{E}{\delta_i^*}$$

and

$$Q = \delta_i^* \left[\frac{d(S/S_w)}{dY} \right]_w$$

By the use of equations (14) and (15), the energy equation can be written as

$$\frac{\overline{T}}{2} \frac{d\left(\tilde{\delta}_i^*\right)^2}{d\tilde{X}} + \left(\tilde{\delta}_i^*\right)^2 \frac{d\overline{T}}{d\tilde{X}} = -Q(S_w) \tag{22}$$

The final equations to be solved simultaneously are equations (16), (19), and (22).

As in reference 2 the velocity and enthalpy profiles are taken from the reverse-flow or "lower branch" solutions of reference 5. Because only a limited number of these solutions are presented in reference 5, it was necessary to obtain additional ones. The additional solutions were obtained by using the programed equations described in reference 17 for $N_{Pr} = 1$ and $\phi = 1$. For these conditions the similar boundary-layer equations of reference 17 reduce to those of reference 5. The equations in reference 17 were obtained by assuming similar flow and using the similarity parameters

$$\psi = f\sqrt{2 \int_0^x \rho_w \mu_w u_e \, dx} \tag{23}$$

$$\eta = \frac{u_e \int_0^y \rho \, dy}{\sqrt{2 \int_0^x \rho_w \mu_w u_e \, dx}} \tag{24}$$

for two-dimensional flow.

The resulting boundary-layer equations are

$$f''' + f(f'') + \beta\left[1 + S - (f')^2\right] = 0 \tag{25}$$

and

$$S'' + S'f = 0 \tag{26}$$

where

$$\beta = \frac{2}{u_e^2} \frac{du_e}{dx} \frac{\int_0^x \rho_w \mu_w u_e \, dx}{t_e \rho_w \mu_w}$$

and

$$f' = \frac{u}{u_e} = \frac{U}{U_e}$$

Solutions to these equations were obtained over a range of negative values of β for $t_w = 0.35$. As in reference 2, the velocity and enthalpy profiles are uncoupled from the parameter β by assuming that the velocity profile is related to the parameter a which is equal to the distance to the point of zero velocity divided by δ $\left(\text{that is, } a = \frac{Y_{u=0}}{\delta}\right)$. Similarly, the enthalpy profile is assumed to be related to the parameter b which is equal to ζ'_w (that is, $b = \zeta'_w$). Therefore, a reverse-flow solution to equations (25) and (26) for a given β and t_w is assumed to be uniquely specified by the associated values of a and b. The integral parameters $\overline{H}$, J, P, $\overline{R}$, and δ_i^* were therefore obtained from the reverse-flow solutions and plotted as functions of the associated values of a. The resulting distributions were fitted with polynomials by using the method of least squares. The coefficients for the polynomials are given in table I where, for example,

$$\overline{H} = c_1 + c_2 a + c_3 a^2 + c_4 a^3 + c_5 a^4 + c_6 a^5 \tag{27}$$

As the parameter E is a function of both the velocity and enthalpy profiles, it is a function of both a and b. Therefore, values of E were curve fitted as functions of a for various values of b and also curve fitted as functions of b for various values of a. The results of this procedure are given in tables II and III. In table III the d coefficients are used to emphasize that E is a polynomial in b for the value of a shown.

The parameters δ_i^* and E shown in the tables are actually integrals over η rather than Y. However, the appearance of these parameters in the final equations is consistent with the original definitions of Q and $\overline{T}$, inasmuch as these parameters always appear as ratios to each other as in $\overline{T}$, or δ_i^* is multiplied by a derivative which can be found with respect to η as in Q. Because E was only available at discrete values of a or b, the values and derivatives of E for given values of a and b were obtained by linear interpolation between the available values.

Examination of equations (16), (19), and (22) shows that the unknowns are now a, b, and $\left(\tilde{\delta}_i^*\right)^2$. The integral parameters are polynomials of power greater than 1, so the resulting set of ordinary differential equations is nonlinear. The boundary conditions at $\tilde{X} = 0$, which is the separation point, are $\tilde{\delta}_i^* = 1$, $a = 0$, and $b = \left(\zeta'_w\right)_{\tilde{X}=0}$. As this latter value is not generally known, it was assumed to be equal to ζ'_w for the enthalpy distribution corresponding to the value of β which gives $f''_w = 0$ (at the separation point). That is, the local enthalpy profile at separation was assumed to be the one associated with the velocity profile at separation, according to reference 5.

APPENDIX A

The equations for a, b, and $\left(\tilde{\delta}_i^*\right)^2$ as functions of $\tilde{X}$ were solved numerically on an IBM electronic data processing machine. The result of the solution, the b distribution, is shown in figure 8 where the ratio $\zeta'_w \Big/ \left(\zeta'_w\right)_{\tilde{X}=0}$ is plotted as a function of $\tilde{X}$. The distribution of this ratio with x can be obtained by application of the inverse of the transformations. By assuming that $\lambda = 1$ and using the value of $\left(\delta_i^*\right)_o$ obtained from the value of δ_i^* at $a = 0$ (velocity profile parameter at separation), the heat-transfer rate was obtained from the expression

$$q = k_w \left(\frac{\partial T}{\partial y}\right)_w = \frac{k_w}{c_p} H_{s,e} \left(\frac{\partial \zeta}{\partial \eta}\right)_w \left(\frac{\partial \eta}{\partial y}\right)_w$$

REFERENCES

1. Carlson, Walter O.: Heat Transfer in Laminar Separated and Wake Flow Regions. 1959 Heat Transfer Fluid Mech. Inst. (Univ. of Calif.), Stanford Univ. Press, June 1959, pp. 140-155.

2. Holden, M. S.: An Analytical Study of Separated Flows Induced by Shock Wave – Boundary Layer Interaction. Rept. No. A1-1972-A-3 (Contract NAS 5-3976), Cornell Aeron. Lab., Inc., Dec. 1965.

3. Reeves, Barry L.; and Lees, Lester: Theory of Laminar Near Wake of Blunt Bodies in Hypersonic Flow. AIAA J., vol. 3, no. 11, Nov. 1965, pp. 2061-2074.

4. Lees, Lester; and Reeves, Barry L.: Supersonic Separated and Reattaching Laminar Flows: I. General Theory and Application to Adiabatic Boundary-Layer/Shock-Wave Interactions. AIAA J., vol. 2, no. 11, Nov. 1964, pp. 1907-1920.

5. Cohen, Clarence B.; and Reshotko, Eli: Similar Solutions for the Compressible Laminar Boundary Layer With Heat Transfer and Pressure Gradient. NACA Rept. 1293, 1956. (Supersedes NACA TN 3325.)

6. Nielsen, Jack N.; Lynes, Larry L.; and Goodwin, Frederick K.: Calculation of Laminar Separation With Free Interaction by the Method of Integral Relations. Part II: Two-Dimensional Supersonic Nonadiabatic Flow and Axisymmetric Supersonic Adiabatic and Nonadiabatic Flows. AFFDL-TR-65-107, Pt. II, U.S. Air Force, Jan. 1966. (Available from DDC as AD 630 765.)

7. Stainback, P. Calvin: Heat-Transfer Measurements at a Mach Number of 8 in the Vicinity of a 90° Interior Corner Alined With the Free-Stream Velocity. NASA TN D-2417, 1964.

8. Schaefer, William T., Jr.: Characteristics of Major Active Wind Tunnels at the Langley Research Center. NASA TM X-1130, 1965.

9. Lyman, Taylor, ed.: Metals Handbook. Volume 1.- Properties and Selection of Metals. 8th ed., Am. Soc. Metals, c.1961, p. 423.

10. Donaldson, I. S.: On the Separation of a Supersonic Flow at a Sharp Corner. AIAA J. vol. 5, no. 6, June 1967, pp. 1086-1088.

11. Zoby, Ernest V.; and Sullivan, Edward M.: Effects of Corner Radius on Stagnation-Point Velocity Gradients on Blunt Axisymmetric Bodies. NASA TM X-1067, 1965.

12. Dennard, John S.; and Spencer, Patricia B.: Ideal-Gas Tables for Oblique-Shock Flow Parameters in Air at Mach Numbers From 1.05 to 12.0. NASA TN D-2221, 1964.

13. Chapman, Dean R.; Kuehn, Donald M.; and Larson, Howard K.: Investigation of Separated Flows in Supersonic and Subsonic Streams With Emphasis on the Effect of Transition. NACA Rept. 1356, 1958. (Supersedes NACA TN 3869.)

14. Chapman, Dean R.: A Theoretical Analysis of Heat Transfer in Regions of Separated Flow. NACA TN 3792, 1956.

15. Weiss, Robert F.: Base Pressure of Slender Bodies in Laminar, Hypersonic Flow. AIAA J., vol. 4, no. 9, Sept. 1966, pp. 1557-1559.

16. Kruse, Robert L.: Transition and Flow Reattachment of the Separated Boundary Layer of an Apollo-Like Bluff Body in Free Flight at Mach Numbers 1 to 9. NASA TN D-4645, 1968.

17. Beckwith, Ivan E.; and Cohen, Nathaniel B.: Application of Similar Solutions to Calculation of Laminar Heat Transfer on Bodies With Yaw and Large Pressure Gradient in High-Speed Flow. NASA TN D-625, 1961.

18. Scott, C. J.; and Eckert, E. R. G.: Heat and Mass Exchange in the Supersonic Base Region. Separated Flows, Pt. I, AGARD CP No. 4, May 1966, pp. 429-478.

TABLE I.- COEFFICIENTS IN POLYNOMIAL CURVE FITS OF INTEGRAL PARAMETERS THAT ARE FUNCTIONS OF a ONLY

Parameter	Coefficients in polynomial fit					
	c_1	c_2	c_3	c_4	c_5	c_6
$\overline{H}$	0.227	-0.283	0.372	-4.729	8.420	-2.984
J	.341	-.314	-1.051	2.360	-7.123	9.357
P	-.036	-.352	-5.377	7.716	0	0
$\overline{R}$	1.386	.565	16.550	-68.680	212.500	-200.300
δ_i^*	2.713	1.004	32.203	-161.200	481.800	-407.200

TABLE II.- COEFFICIENTS IN POLYNOMIAL CURVE FITS OF INTEGRAL PARAMETER E(a,b) AT VARIOUS CONSTANT VALUES OF b

Value of b	Coefficients in polynomial fit of E(a,b)					
	c_1	c_2	c_3	c_4	c_5	c_6
0.194	-0.192	0.431	0.936	3.142	-13.810	9.088
.174	-.242	.377	3.276	-7.842	9.504	-9.533
.164	-.273	.685	-1.000	15.730	-41.110	27.860
.155	-.304	.618	.345	10.310	-29.940	18.490
.130	-.418	.784	.324	10.670	-24.800	8.555
.116	-.508	.996	-1.578	20.840	-40.330	13.970
.095	-.686	.960	1.148	7.246	-.737	-25.730
.081	-.846	1.047	2.665	-4.069	37.890	-65.750
.068	-1.051	1.376	-1.716	25.000	-28.410	-11.440
.079	-1.485	1.200	5.099	-21.560	113.600	-147.200
.029	-2.177	-.123	31.180	-176.400	499.100	-467.800
.018	-2.936	.551	22.650	-132.800	411.800	-393.000

TABLE III.- COEFFICIENTS IN POLYNOMIAL CURVE FITS OF INTEGRAL PARAMETER E(a,b) AT VARIOUS CONSTANT VALUES OF a

Value of a	Coefficients in polynomial fit of E(a,b)					
	d_1	d_2	d_3	d_4	d_5	d_6
0	-4.694	123.00	-1666	12 436	-47 483	72 052
.106	-4.717	141.30	-2143	17 516	-71 831	115 338
.145	-4.393	128.20	-1879	14 996	-60 586	96 410
.176	-4.203	122.20	-1750	13 579	-53 457	83 202
.247	-3.835	115.70	-1634	12 362	-47 576	72 767
.282	-3.650	117.20	-1722	13 412	-52 817	82 290
.330	-3.305	116.50	-1789	14 218	-56 364	87 713
.357	-2.980	110.50	-1717	13 595	-53 396	82 243
.384	-2.637	105.80	-1719	14 051	-56 634	89 241
.422	-1.952	88.22	-1497	12 481	-50 788	80 478
.474	-1.029	57.51	-1049	9 050	-37 471	59 903
.518	-.432	35.45	-726	6 711	-29 274	48 780

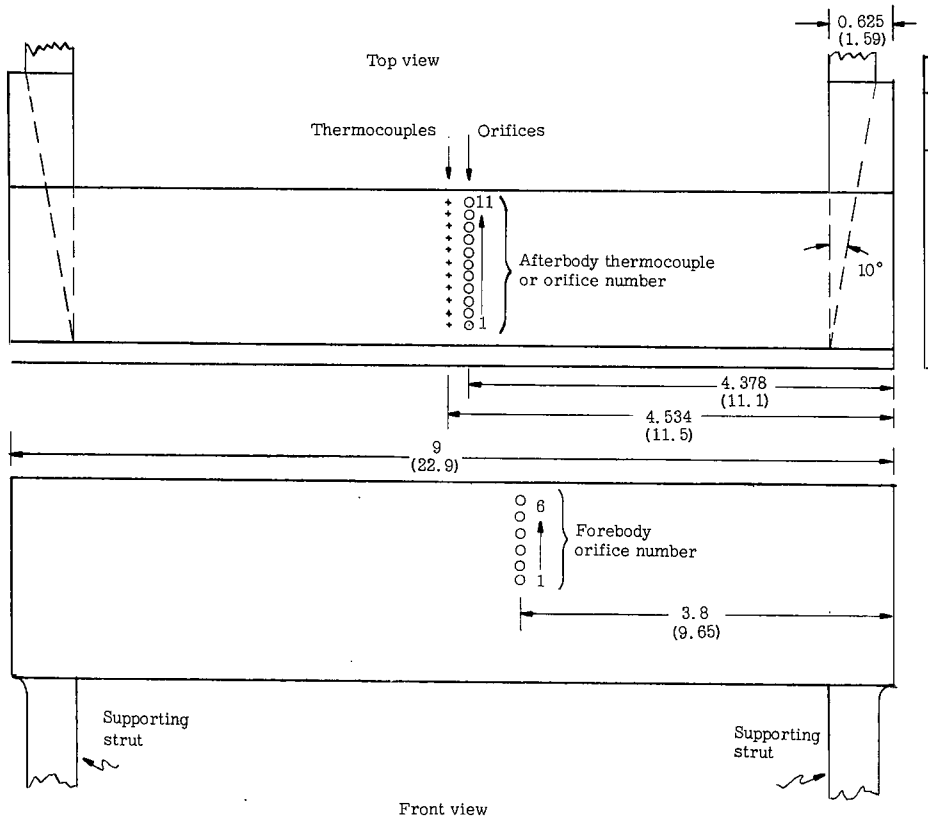

Face instrumentation		Afterbody instrumentation	
Orifice number	θ, deg	Thermocouple or orifice number	l, in. (cm)
1	0	1	0.200 (0.508)
2	3.8	2	.346 (0.879)
3	7.6	3	.492 (1.250)
4	11.4	4	.638 (1.620)
5	15.2	5	.784 (1.991)
6	19.0	6	.930 (2.362)
		7	1.076 (2.733)
		8	1.222 (3.104)
		9	1.368 (3.475)
		10	1.514 (3.846)
		11	1.660 (4.216)

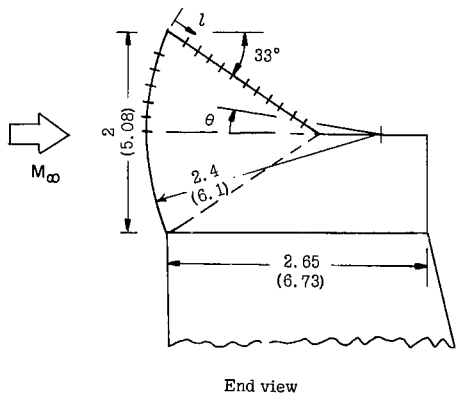

(a) Model sketches showing locations of instrumentation. (All linear dimensions are given in inches and parenthetically in centimeters.)

Figure 1.- Test configuration.

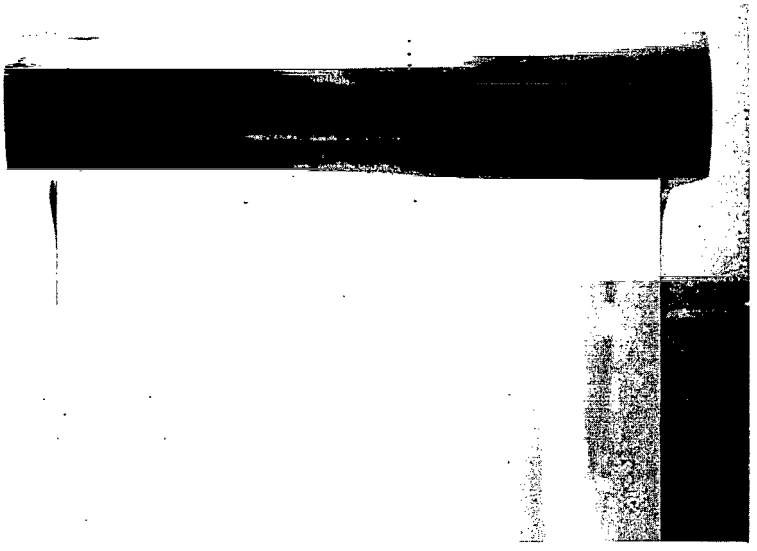

Front view

Oblique view

(b) Photographs of model. L-67-8727

Figure 1.- Concluded.

$R_{\infty, D} = 1.27 \times 10^5$

$R_{\infty, D} = 2.76 \times 10^5$

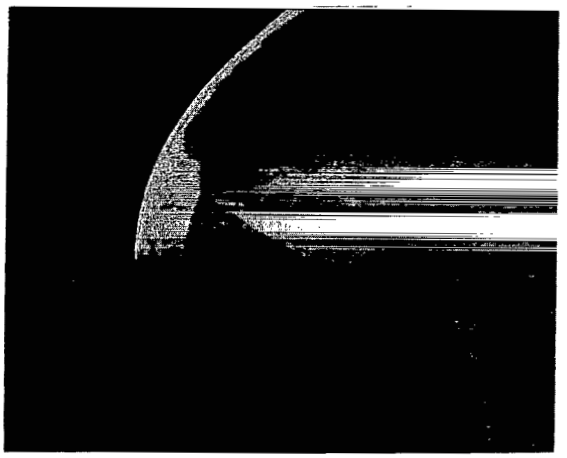

$R_{\infty, D} = 4.65 \times 10^5$

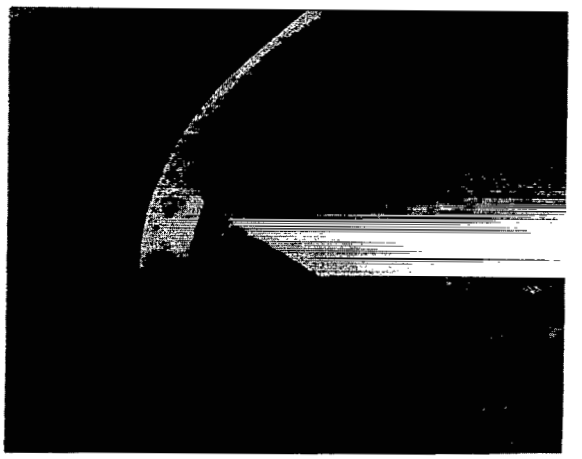

$R_{\infty, D} = 6.55 \times 10^5$

Figure 2.- Schlieren photographs of model flow field for various values of free-stream Reynolds number. L-67-8728

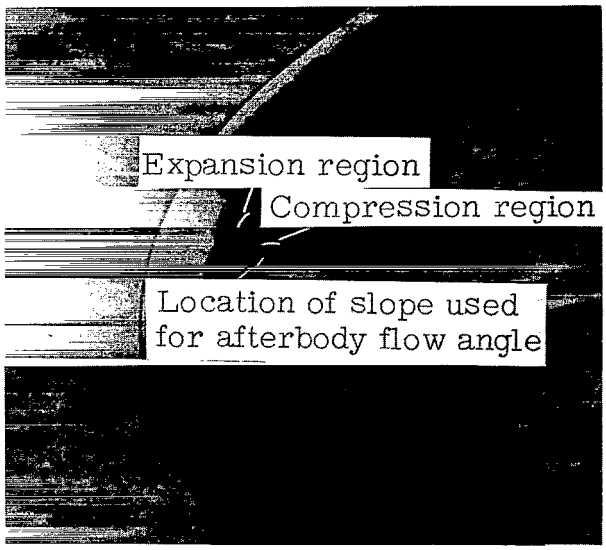

(a) Typical schlieren photograph showing regions of flow field in vicinity of corner.

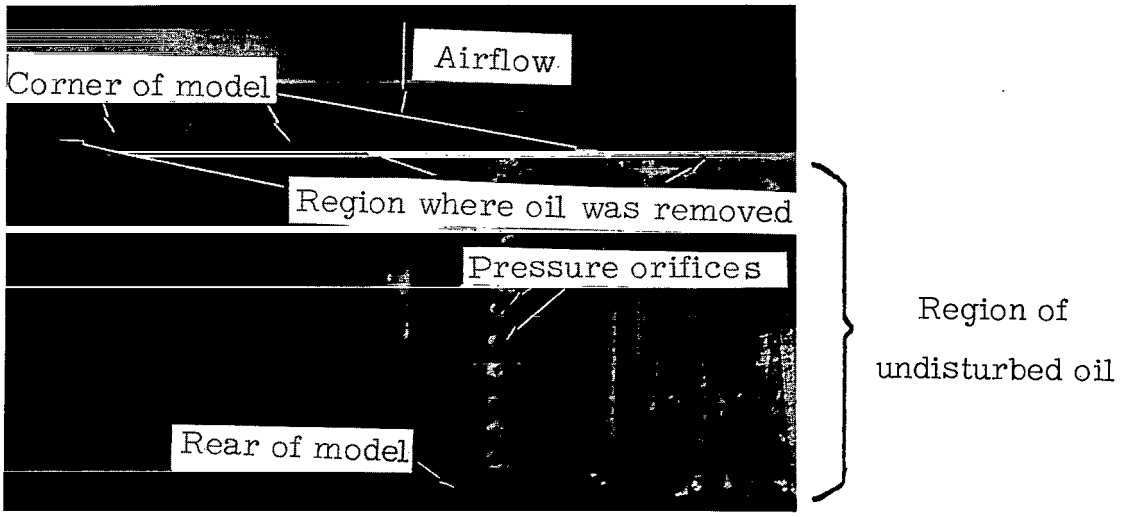

(b) Photograph of oil flow over afterbody.

L-67-8729

Figure 3.- Photographs showing various flow regions and oil flow over afterbody.

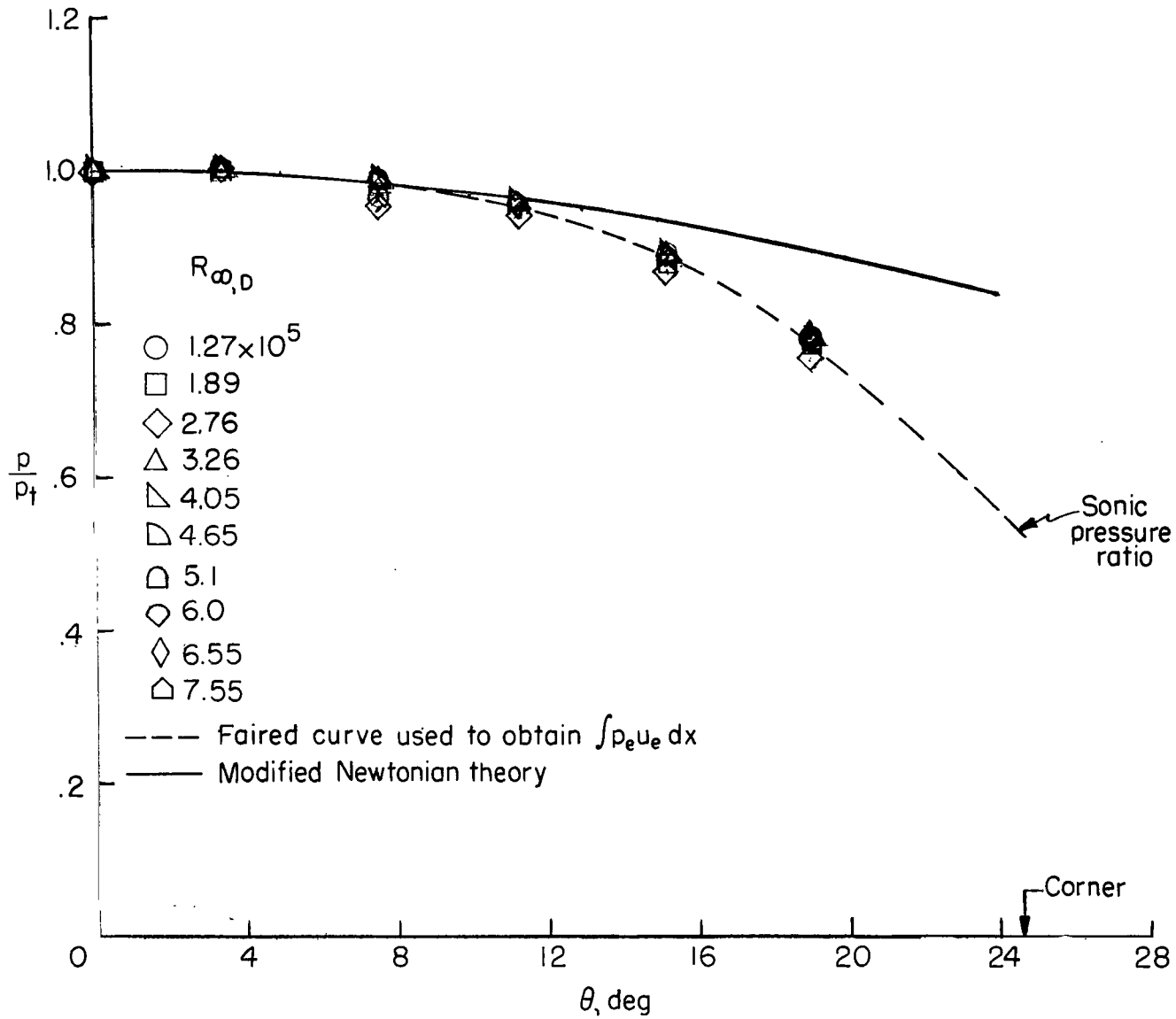

Figure 4.- Pressure distribution over face of model.

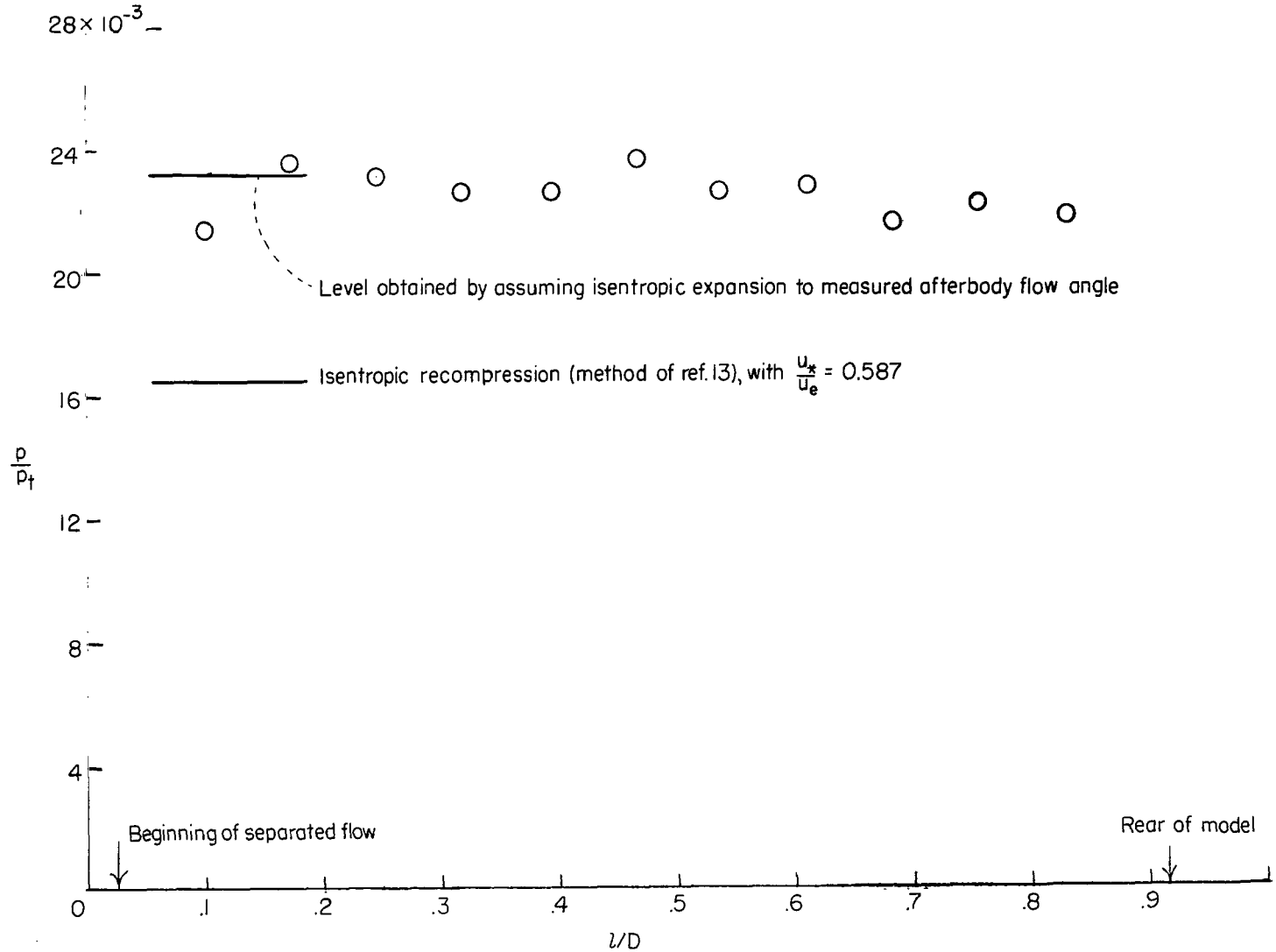

(a) $R_{\infty,D} = 1.89 \times 10^5$.

Figure 5.- Afterbody pressure distributions.

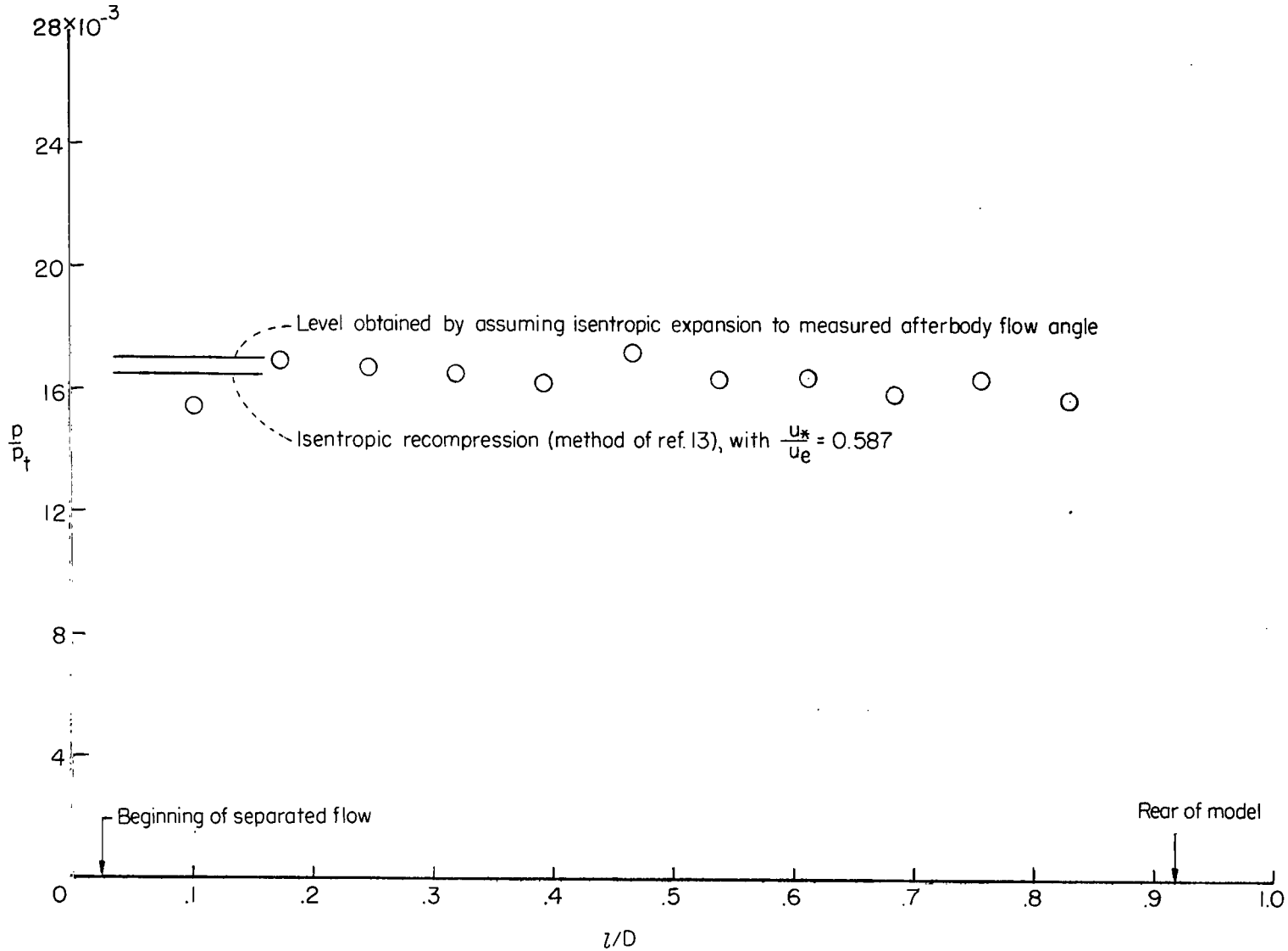

(b) $R_{\infty,D} = 4.05 \times 10^5$.

Figure 5.- Continued.

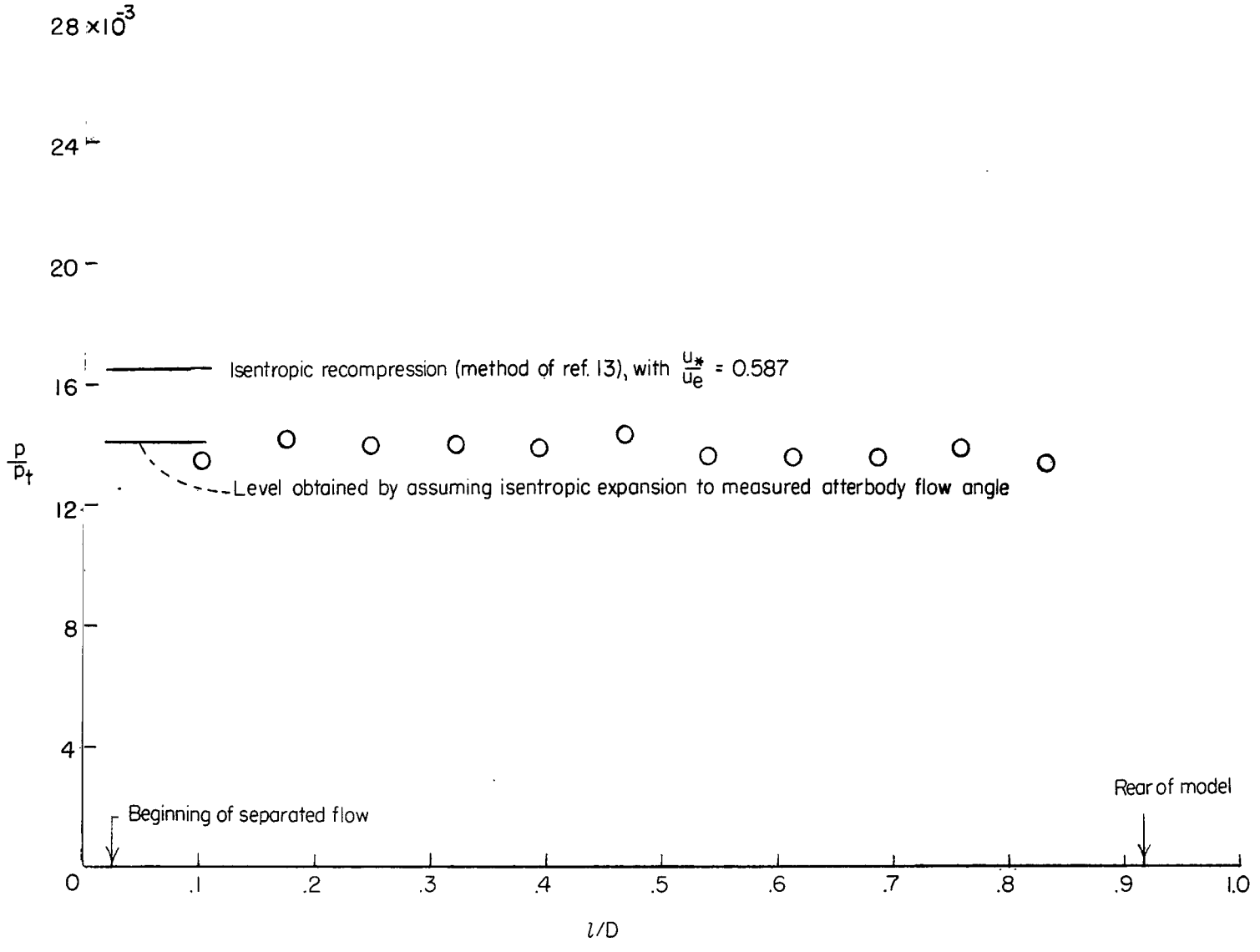

(c) $R_{\infty,D} = 7.55 \times 10^5$.

Figure 5.- Concluded.

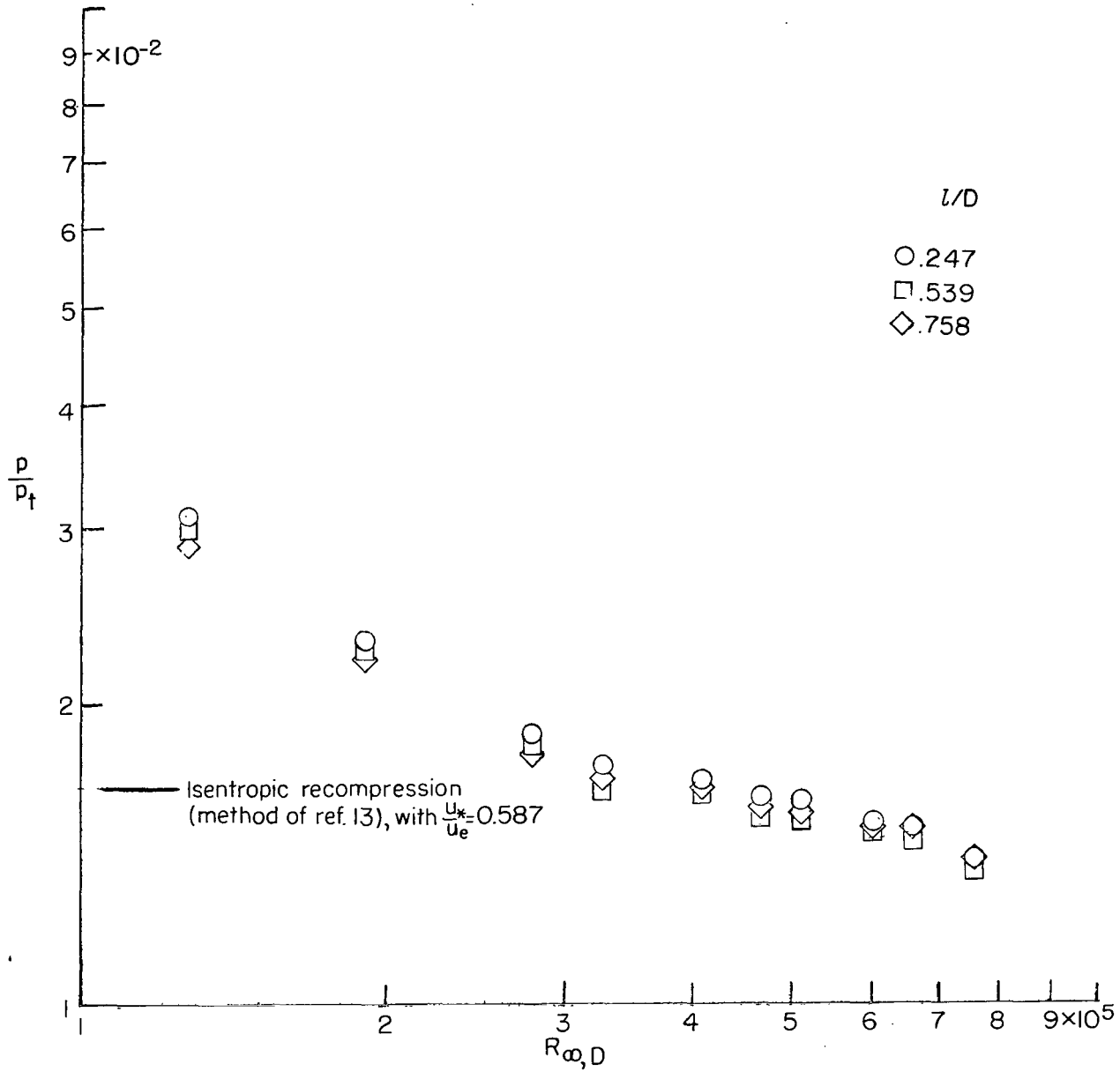

Figure 6.- Variation of afterbody pressure level with free-stream Reynolds number.

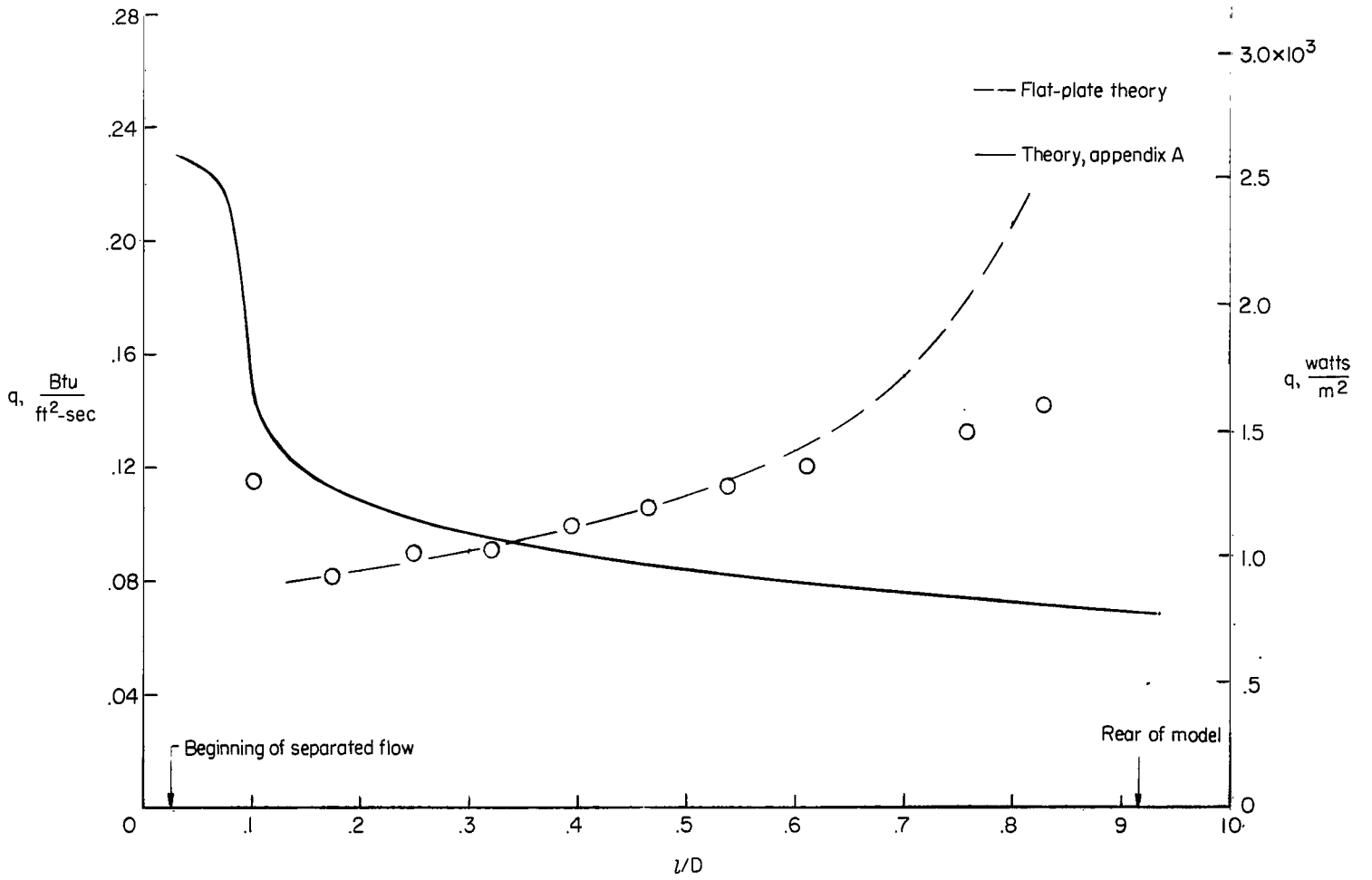

(a) $R_{\infty,D} = 1.27 \times 10^5$; $t_w = 0.44$; $p/p_t = 0.030$ for afterbody flow.

Figure 7.- Afterbody heat-transfer distributions in separated-flow region.

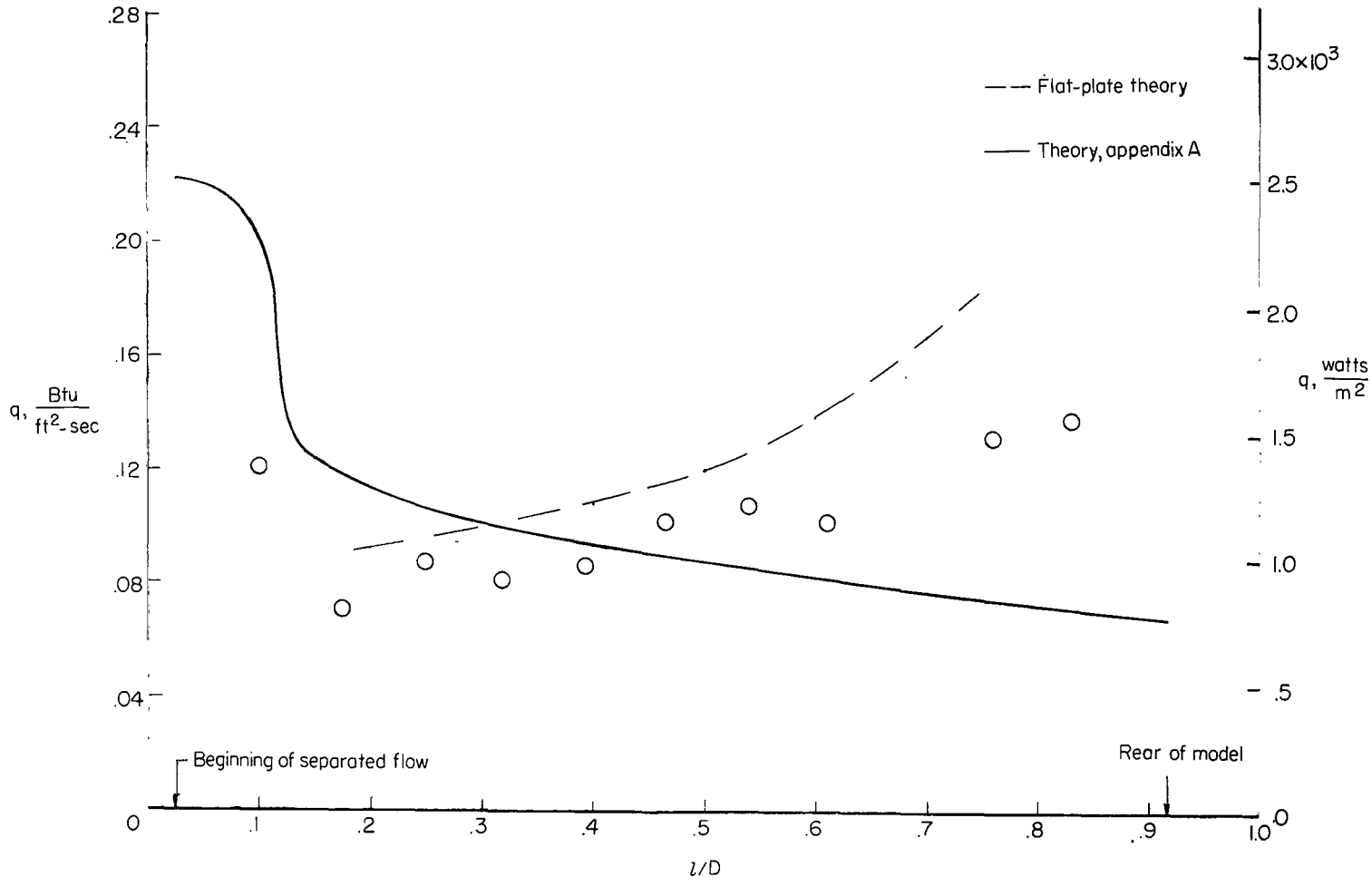

(b) $R_{\infty,D} = 1.89 \times 10^5$; $t_w = 0.429$; $p/p_t = 0.0225$ for afterbody flow.

Figure 7.- Continued.

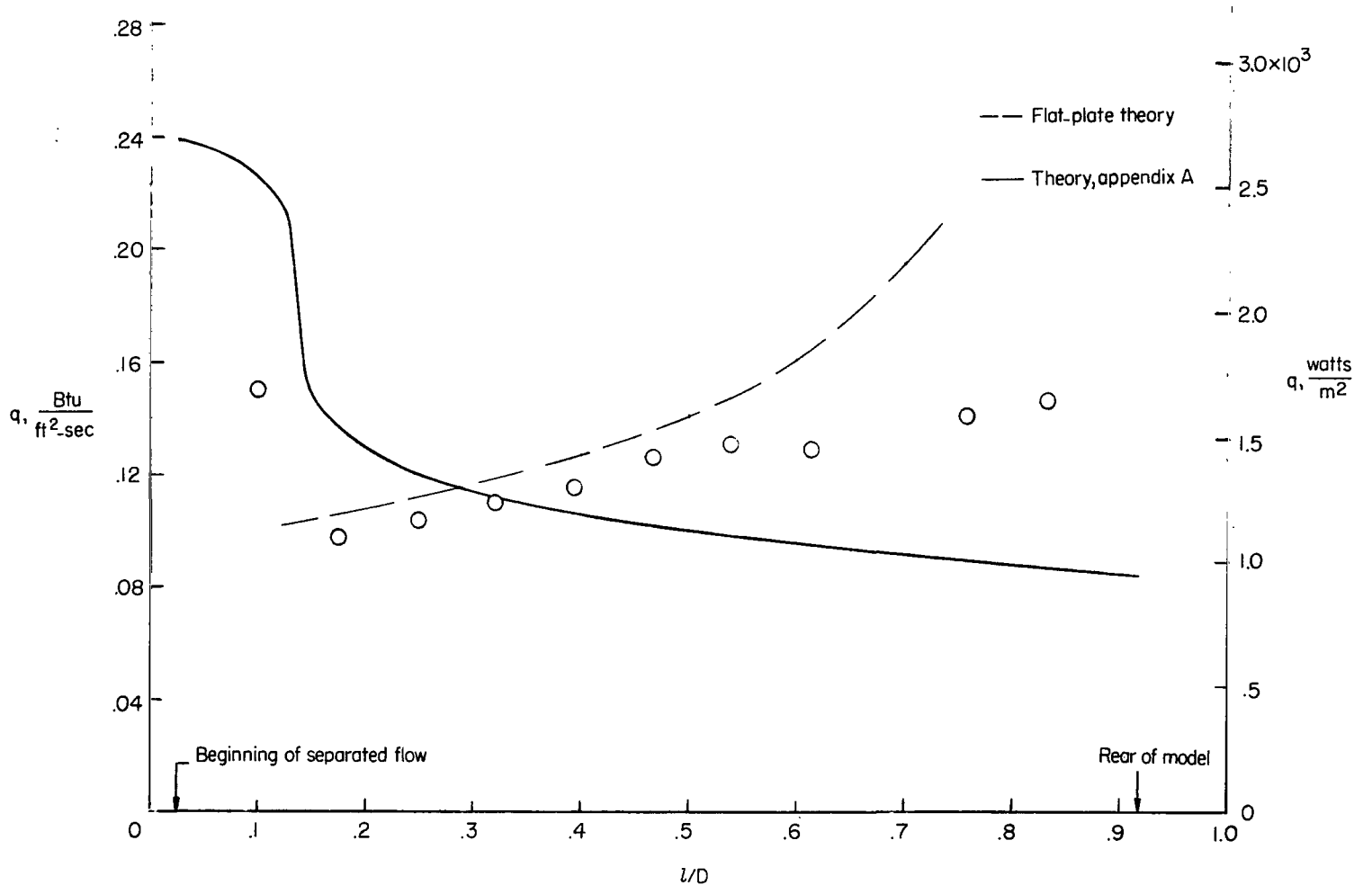

(c) $R_{\infty,D} = 2.76 \times 10^5$; $t_w = 0.415$; $p/p_t = 0.018$ for afterbody flow.

Figure 7.- Continued.

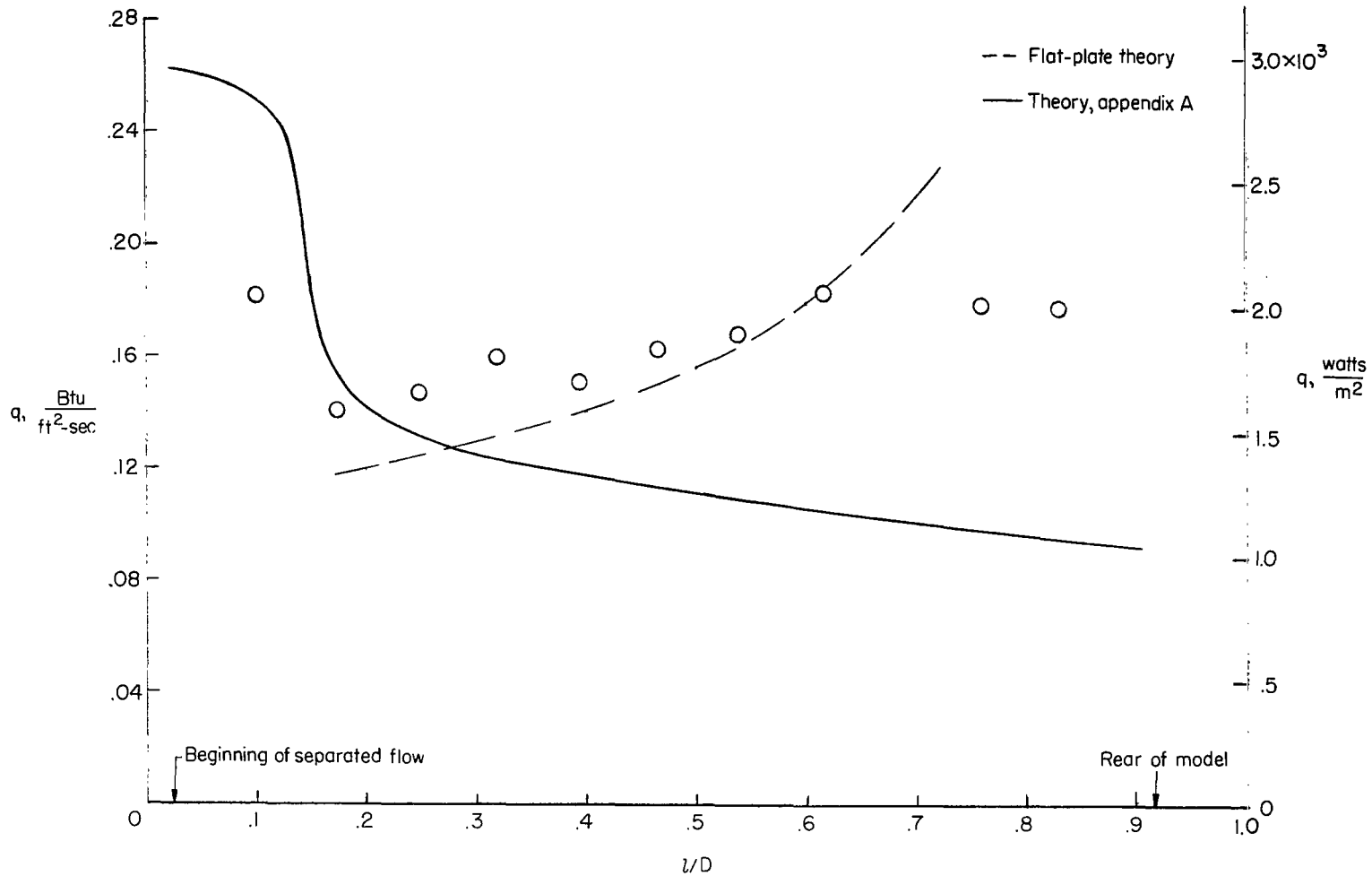

(d) $R_{\infty,D} = 3.26 \times 10^5$; $t_w = 0.404$; $p/p_t = 0.017$ for afterbody flow.

Figure 7.- Continued.

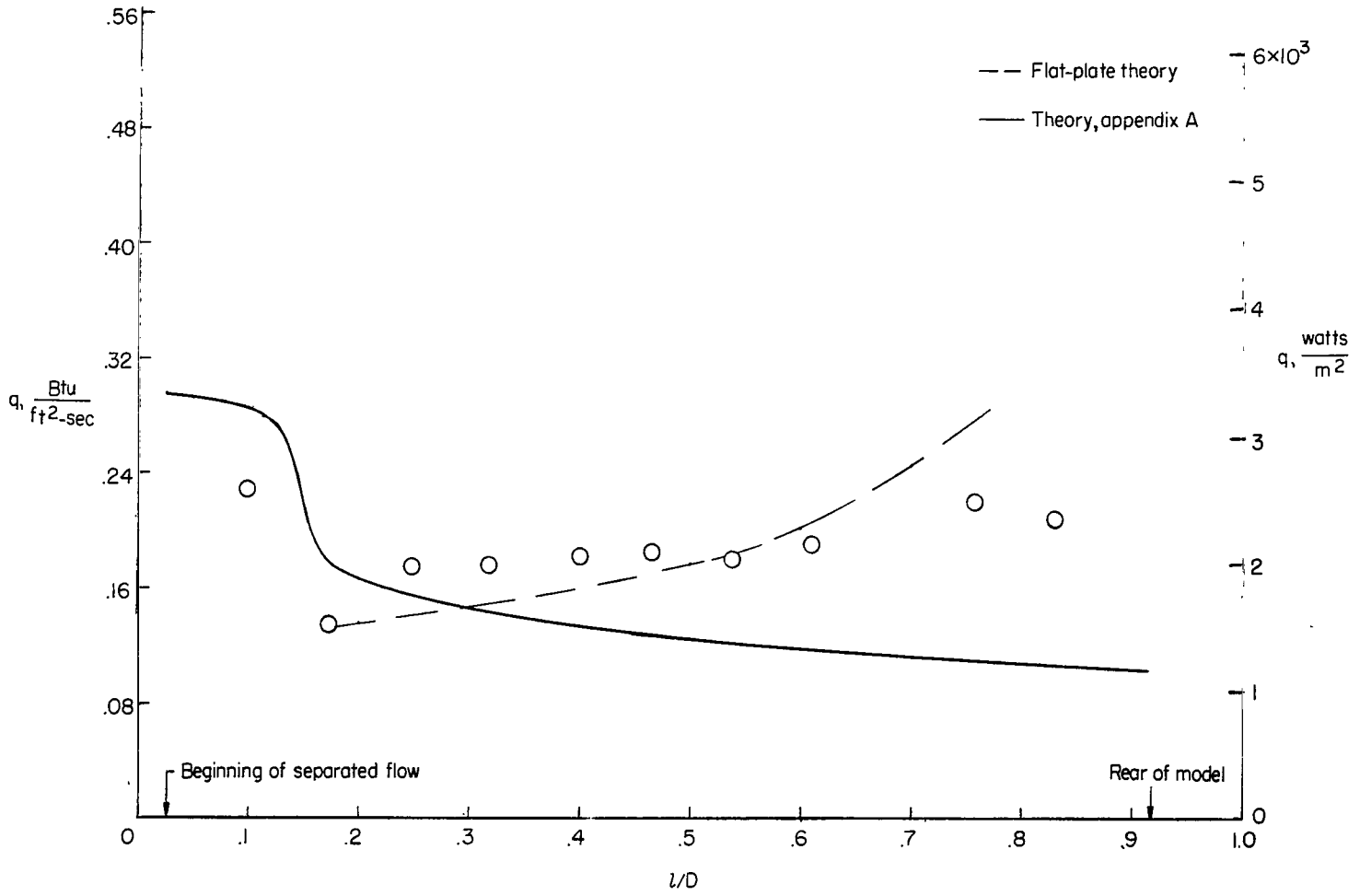

(e) $R_{\infty,D} = 4.05 \times 10^5$; $t_w = 0.397$; $p/p_t = 0.0165$ for afterbody flow.

Figure 7.- Continued.

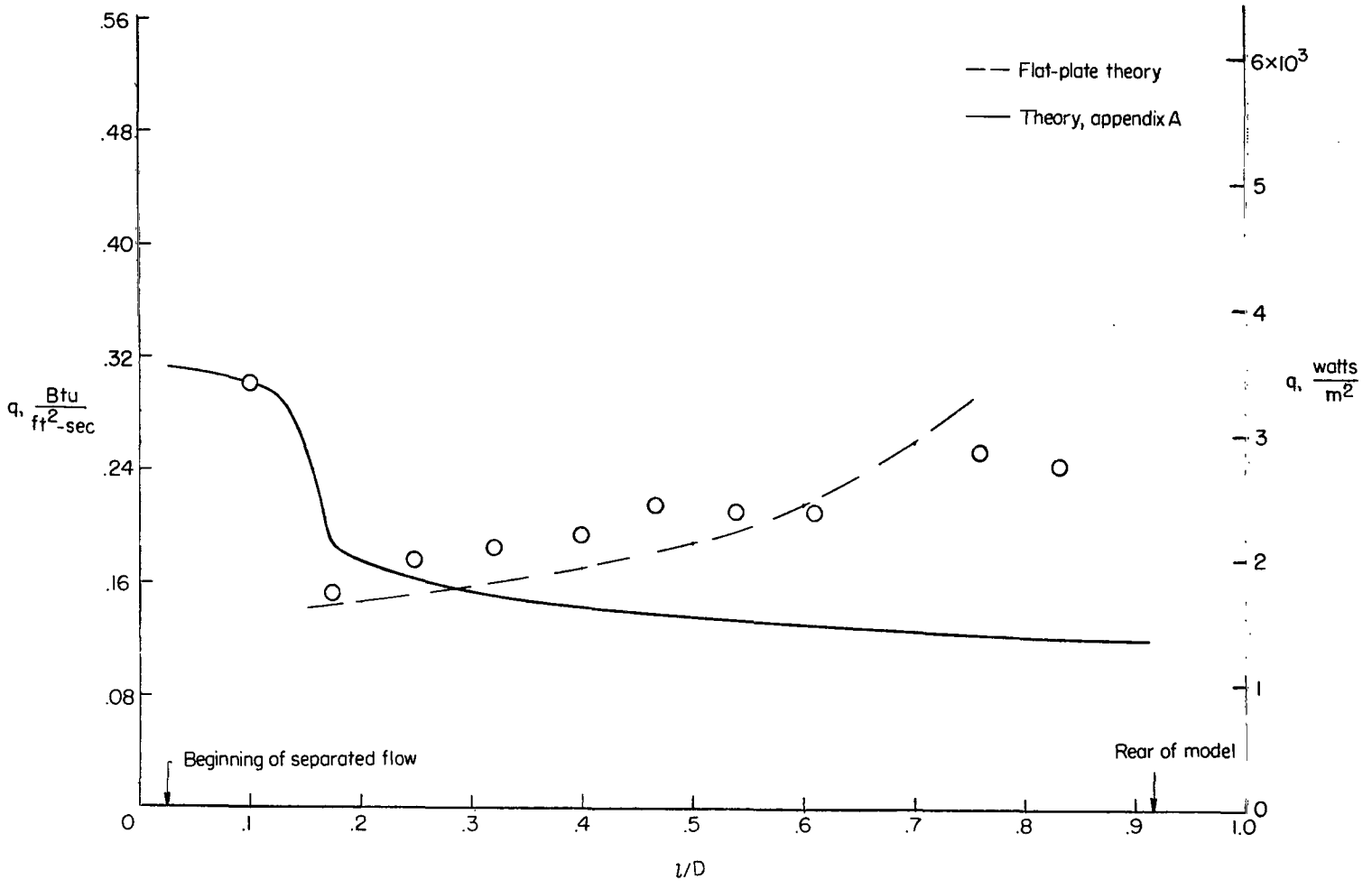

(f) $R_{\infty,D} = 4.65 \times 10^5$; $t_w = 0.394$; $p/p_t = 0.016$ for afterbody flow.

Figure 7.- Continued.

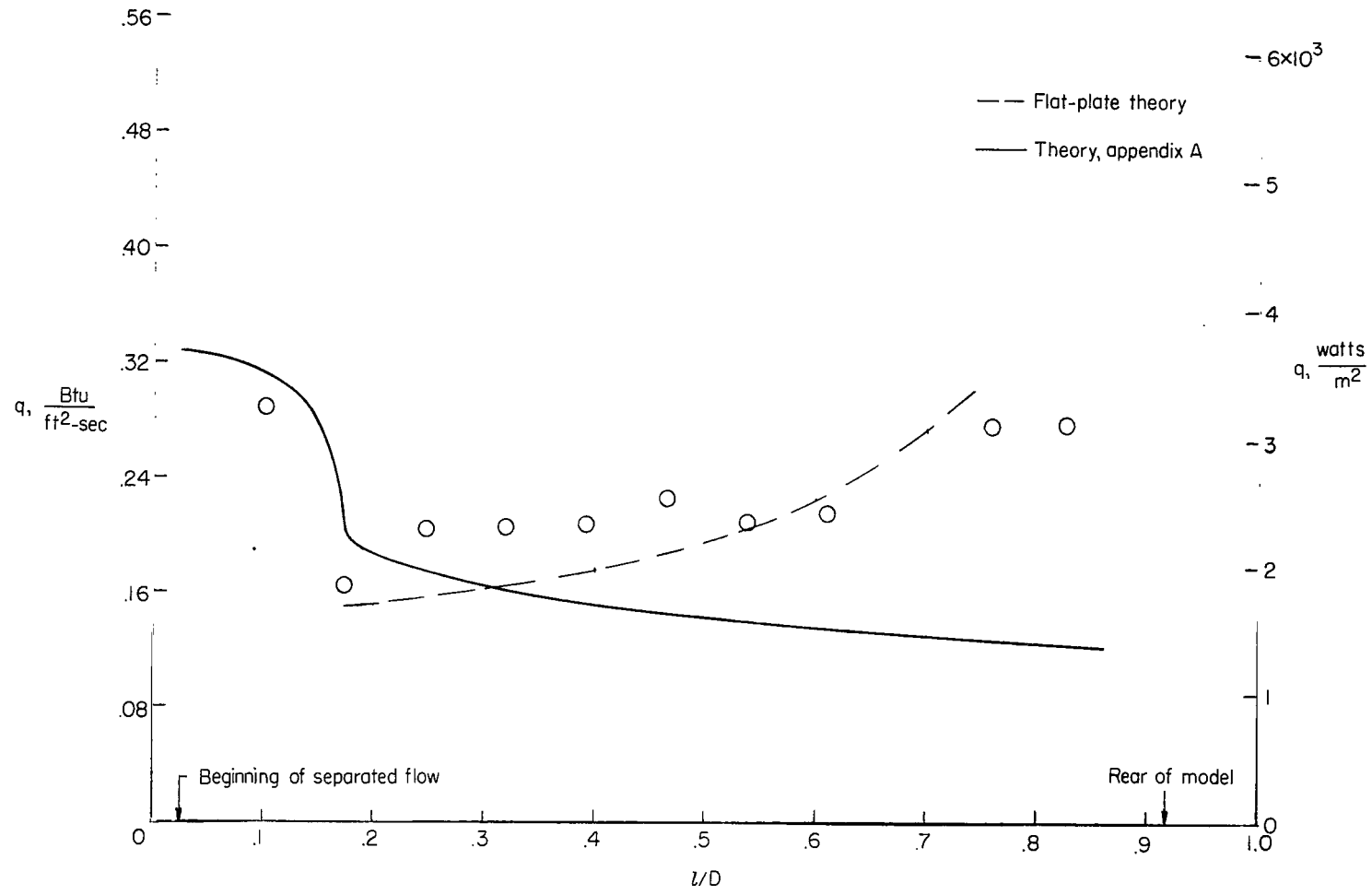

(g) $R_{\infty,D} = 5.1 \times 10^5$; $t_w = 0.391$; $p/p_t = 0.0155$ for afterbody flow.

Figure 7.- Continued.

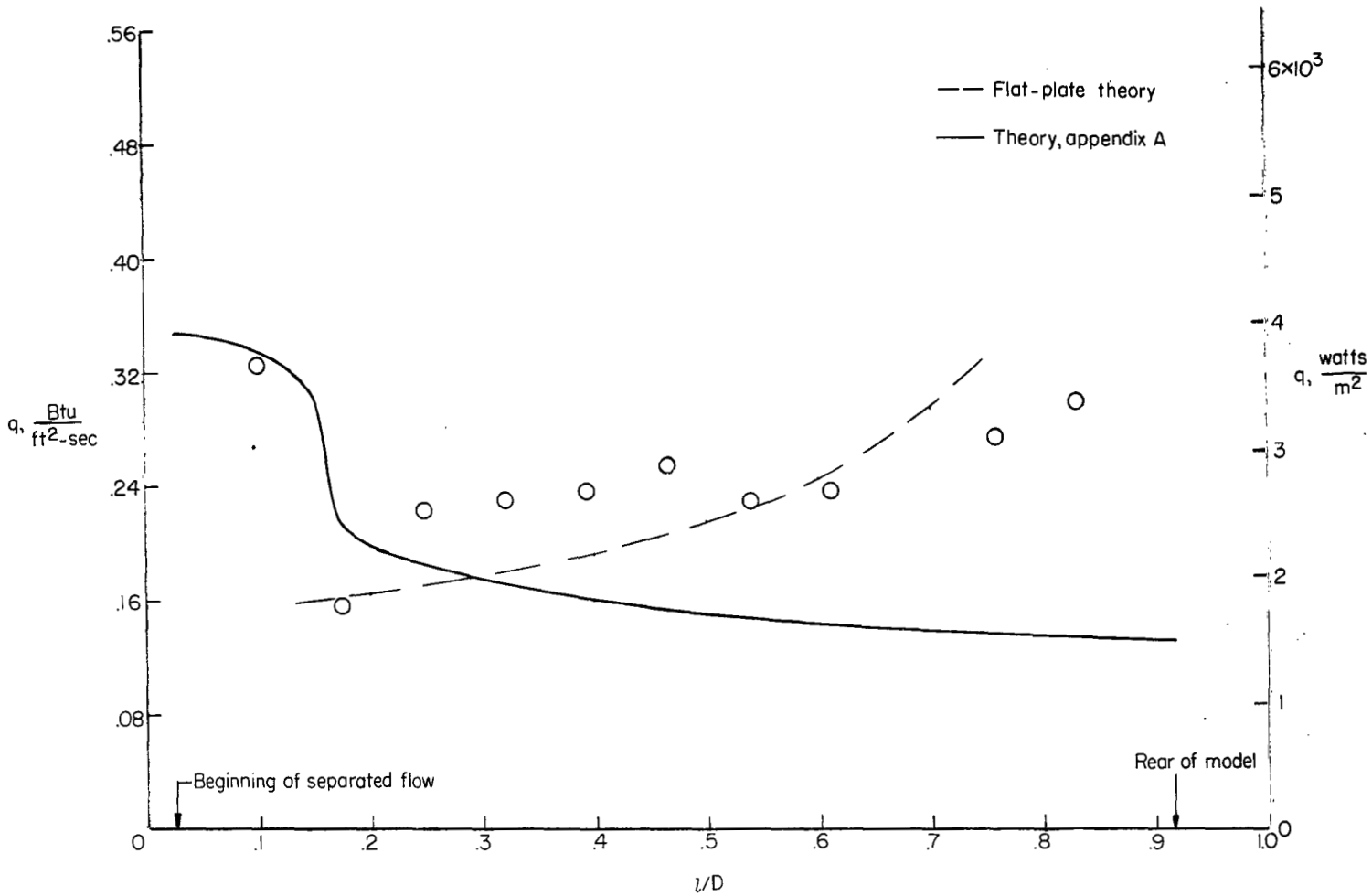

(h) $R_{\infty,D} = 6.0 \times 10^5$; $t_w = 0.39$; $p/p_t = 0.0152$ for afterbody flow.

Figure 7.- Continued.

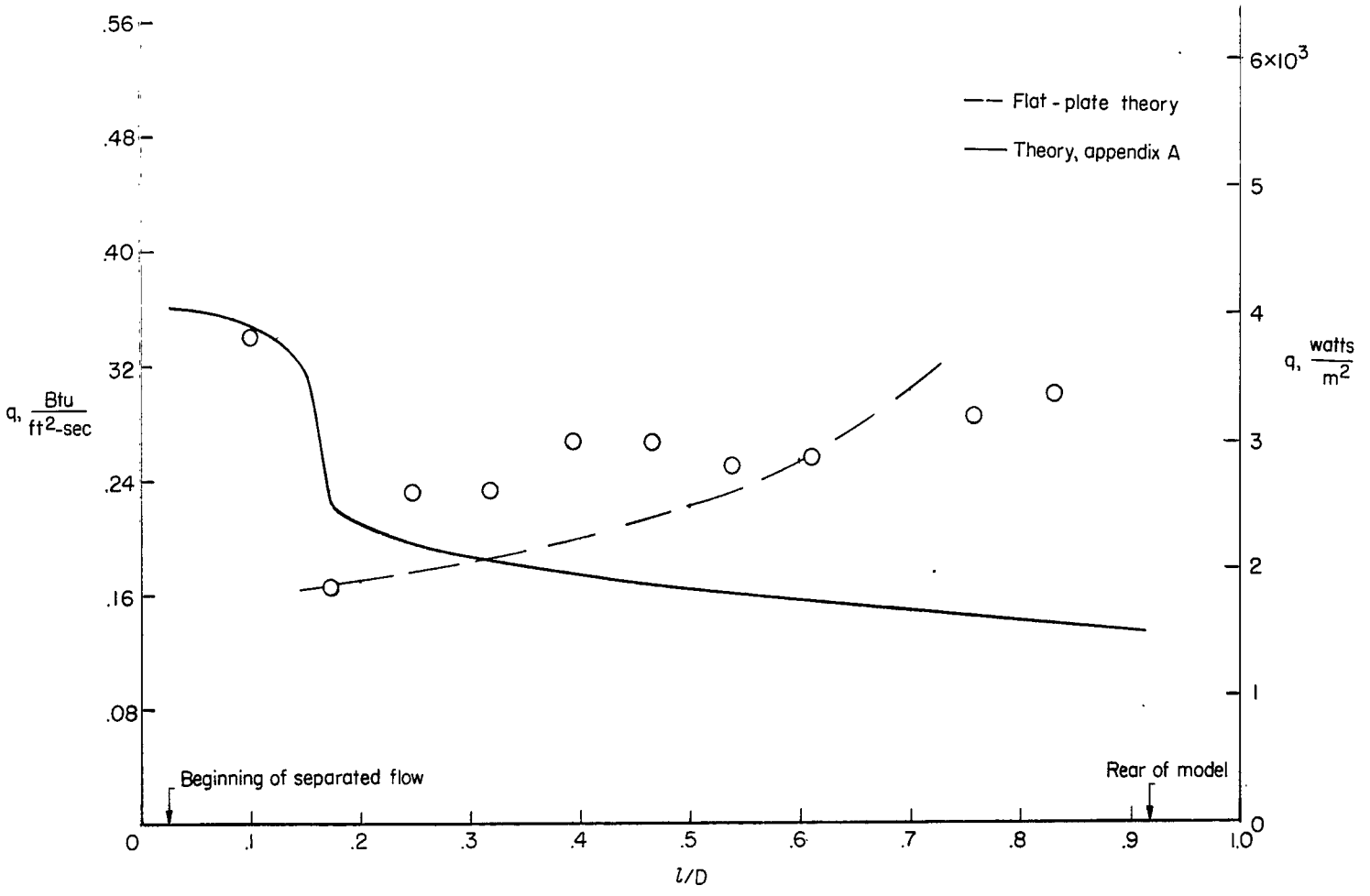

(i) $R_{\infty,D} = 6.55 \times 10^5$; $t_w = 0.39$; $p/p_t = 0.015$ for afterbody flow.

Figure 7.- Continued.

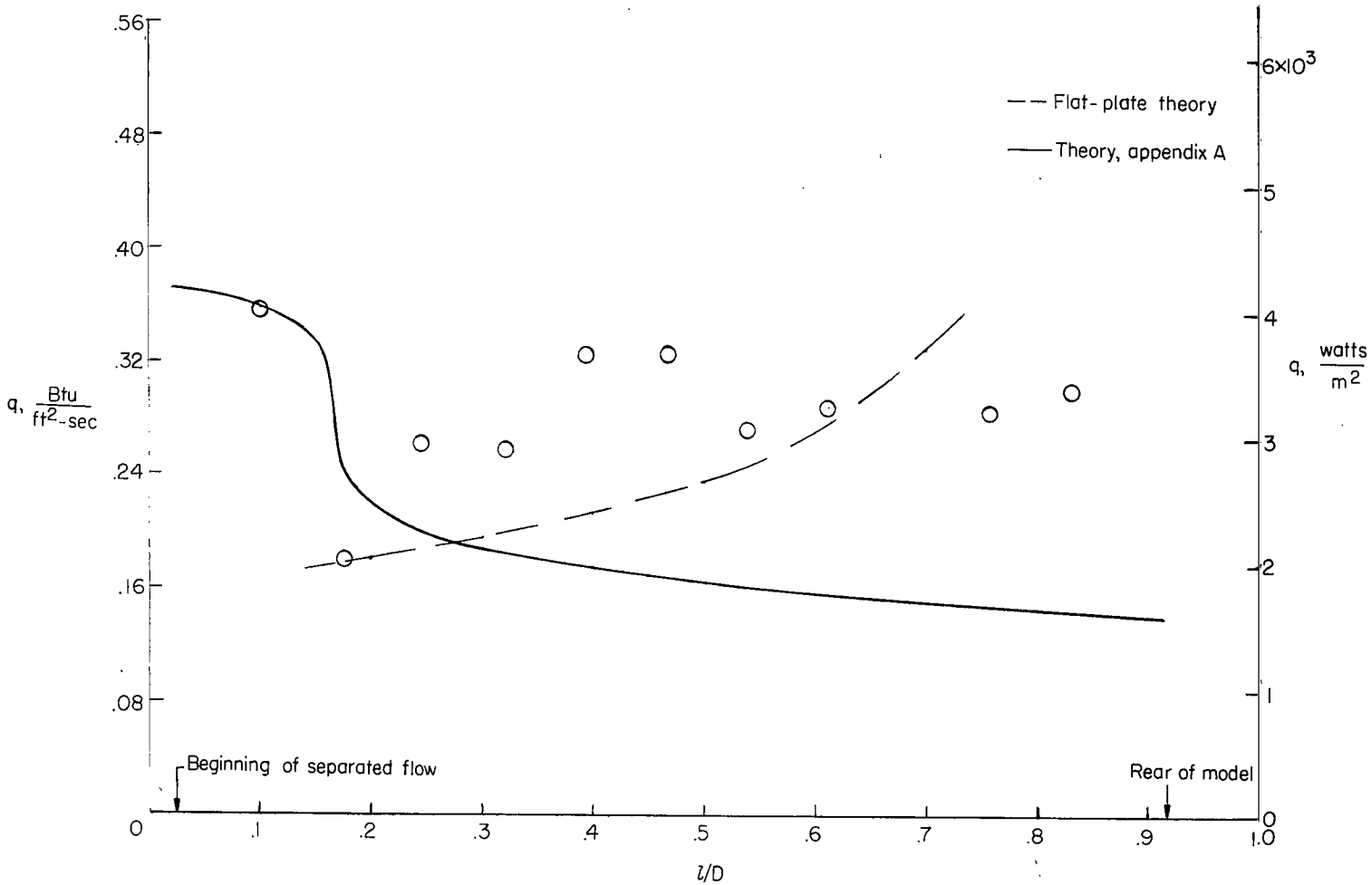

(j) $R_{\infty,D} = 7.55 \times 10^5$; $t_w = 0.386$; $p/p_t = 0.014$ for afterbody flow.

Figure 7.- Concluded.

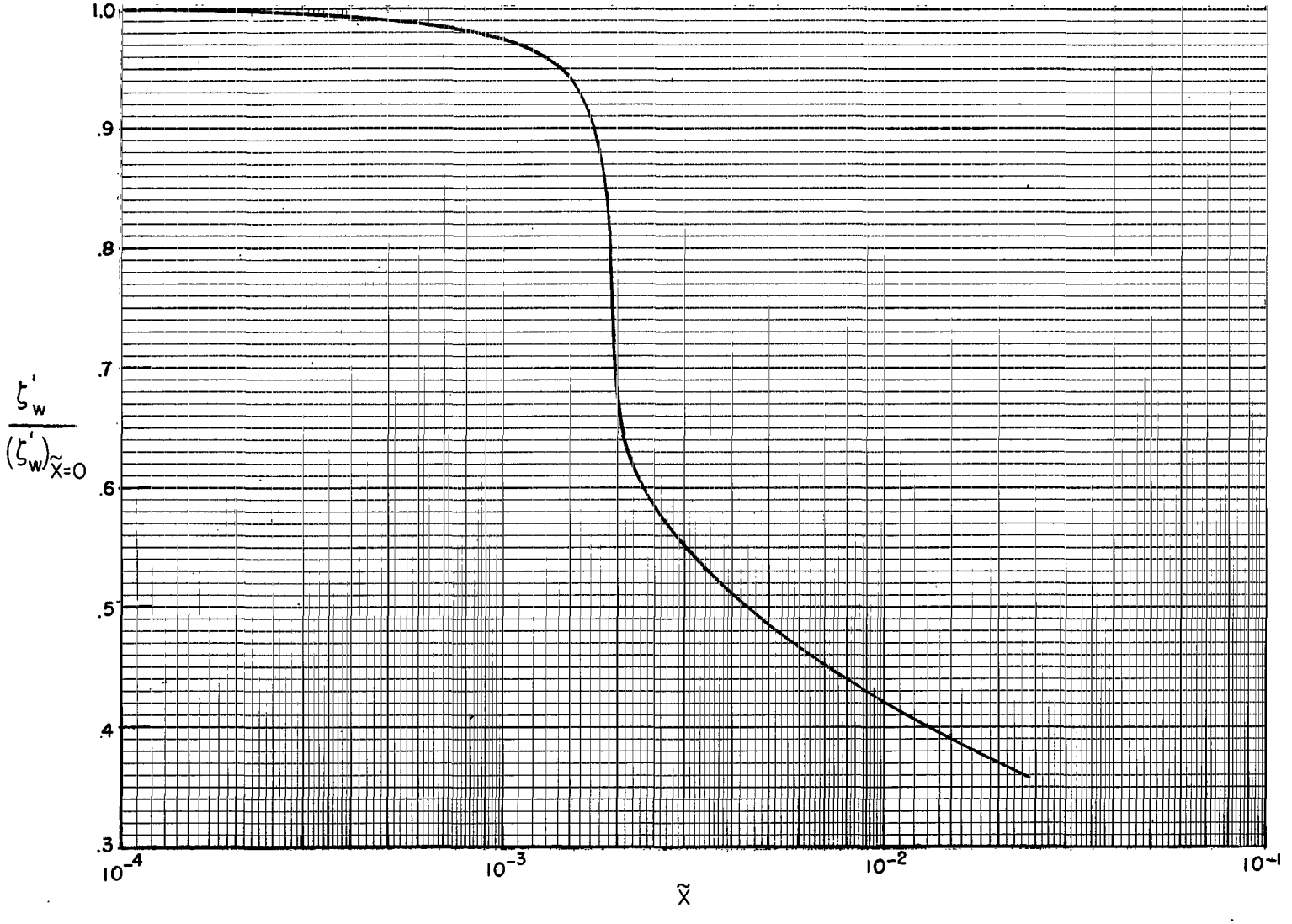

Figure 8.- Wall enthalpy gradient as a function of $\tilde{X}$ from solution to equations (16), (19), and (22) for $t_w = 0.35$.

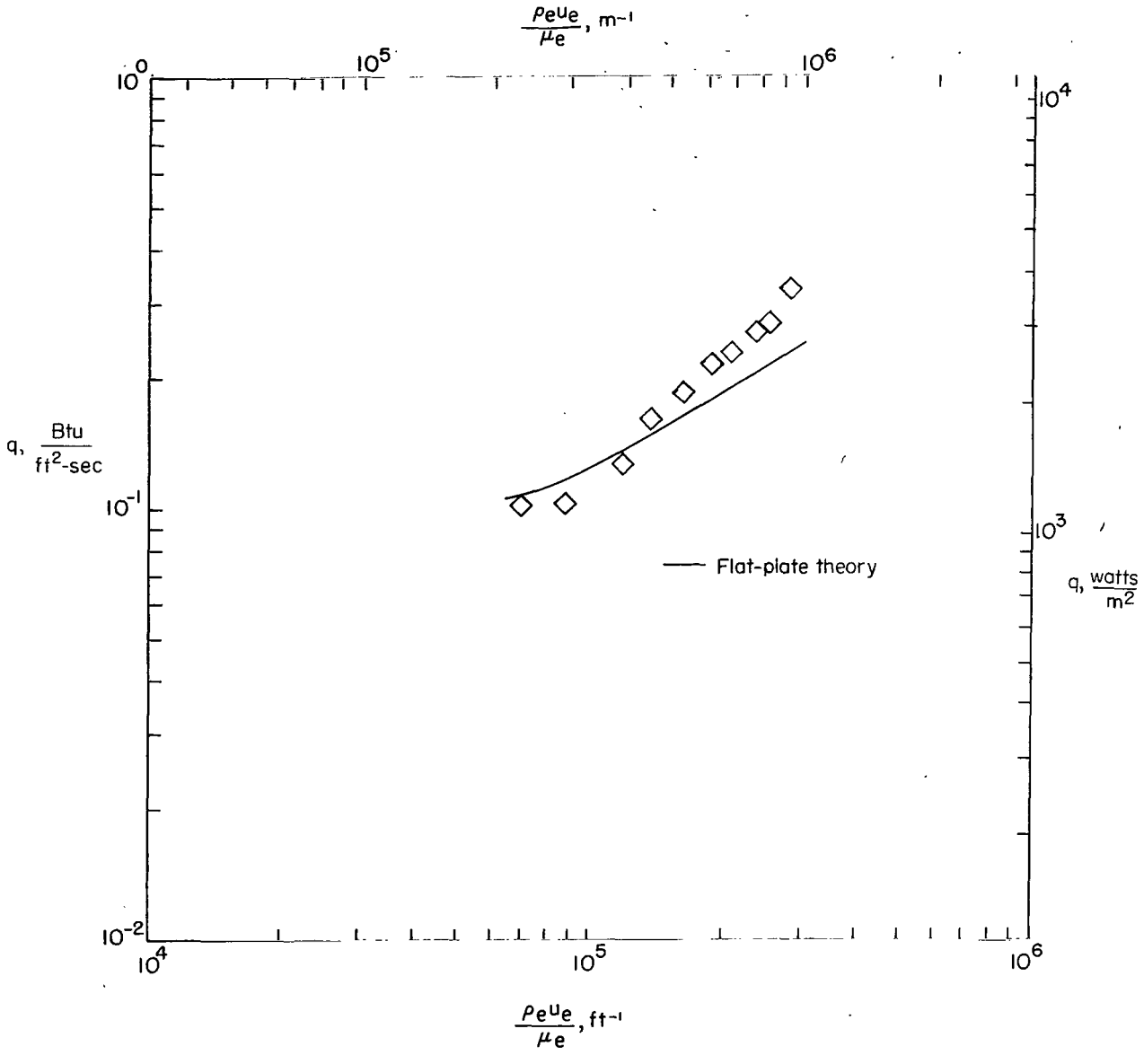

Figure 9.- Variation of heating rate at $\ell/D = 0.47$ with local unit Reynolds number.

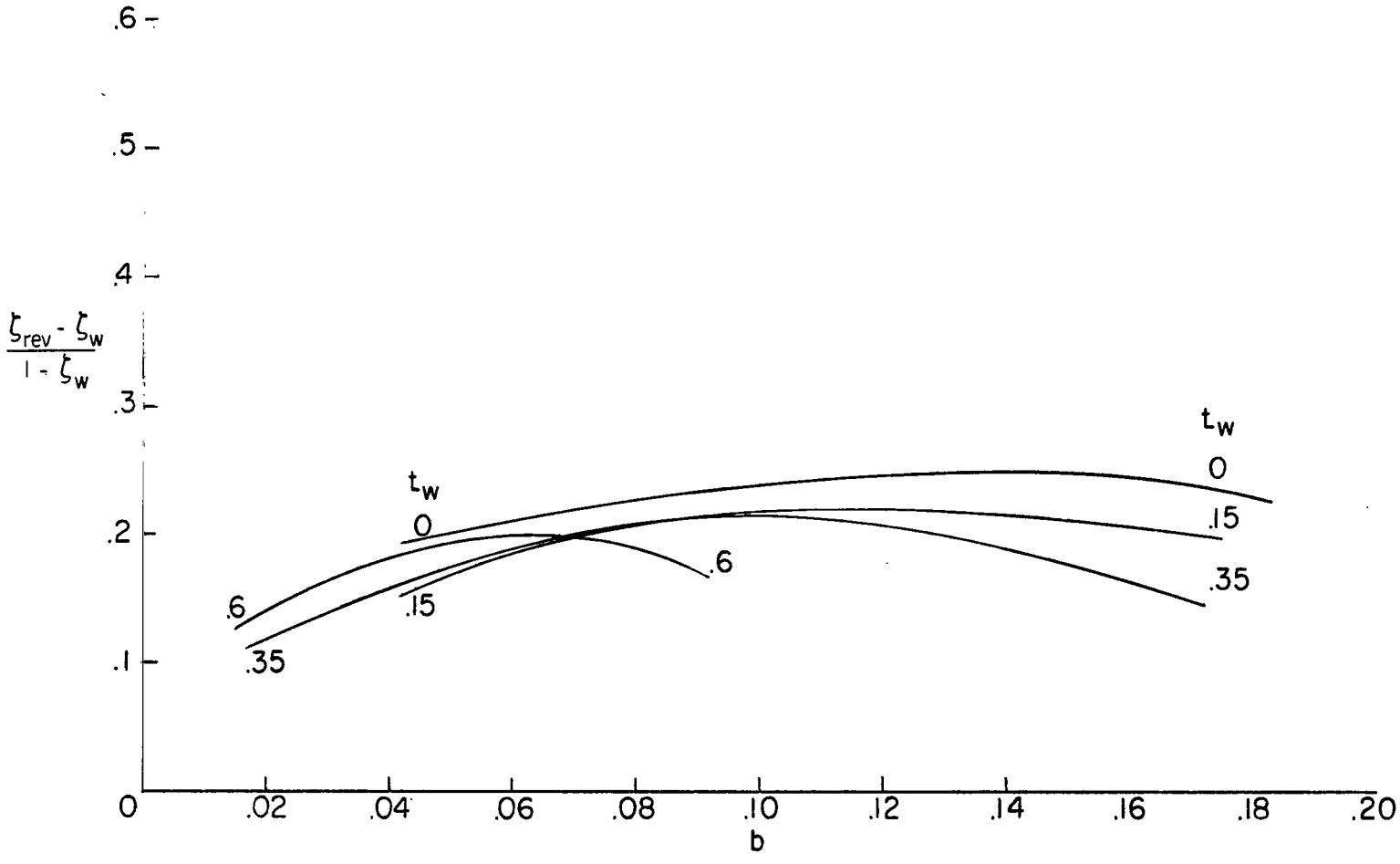

(a) Reverse-flow stagnation enthalpy.

Figure 10.- Variation of maximum reverse-flow velocity and corresponding stagnation enthalpy.

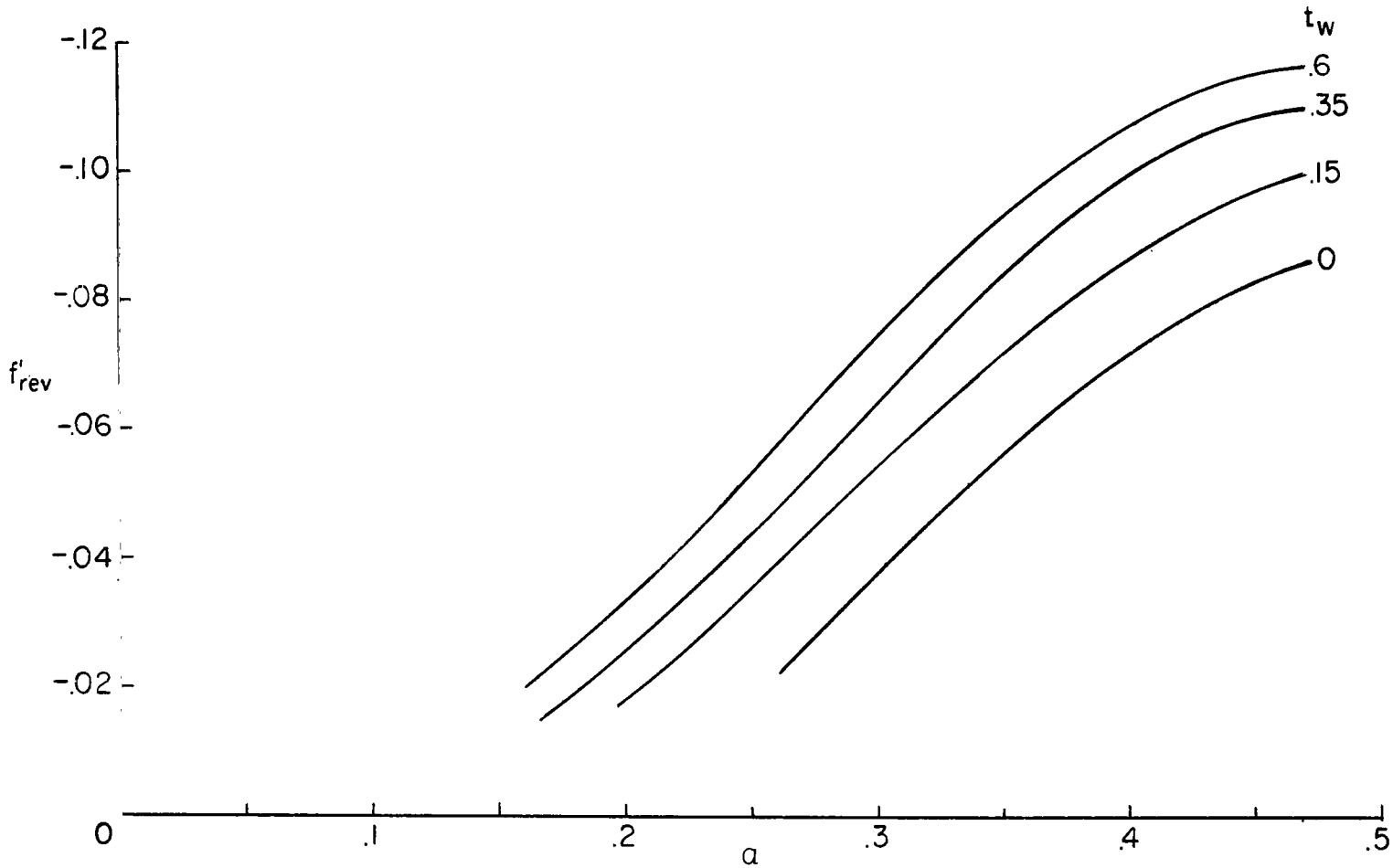

(b) Maximum reverse-flow velocity.

Figure 10.- Concluded.

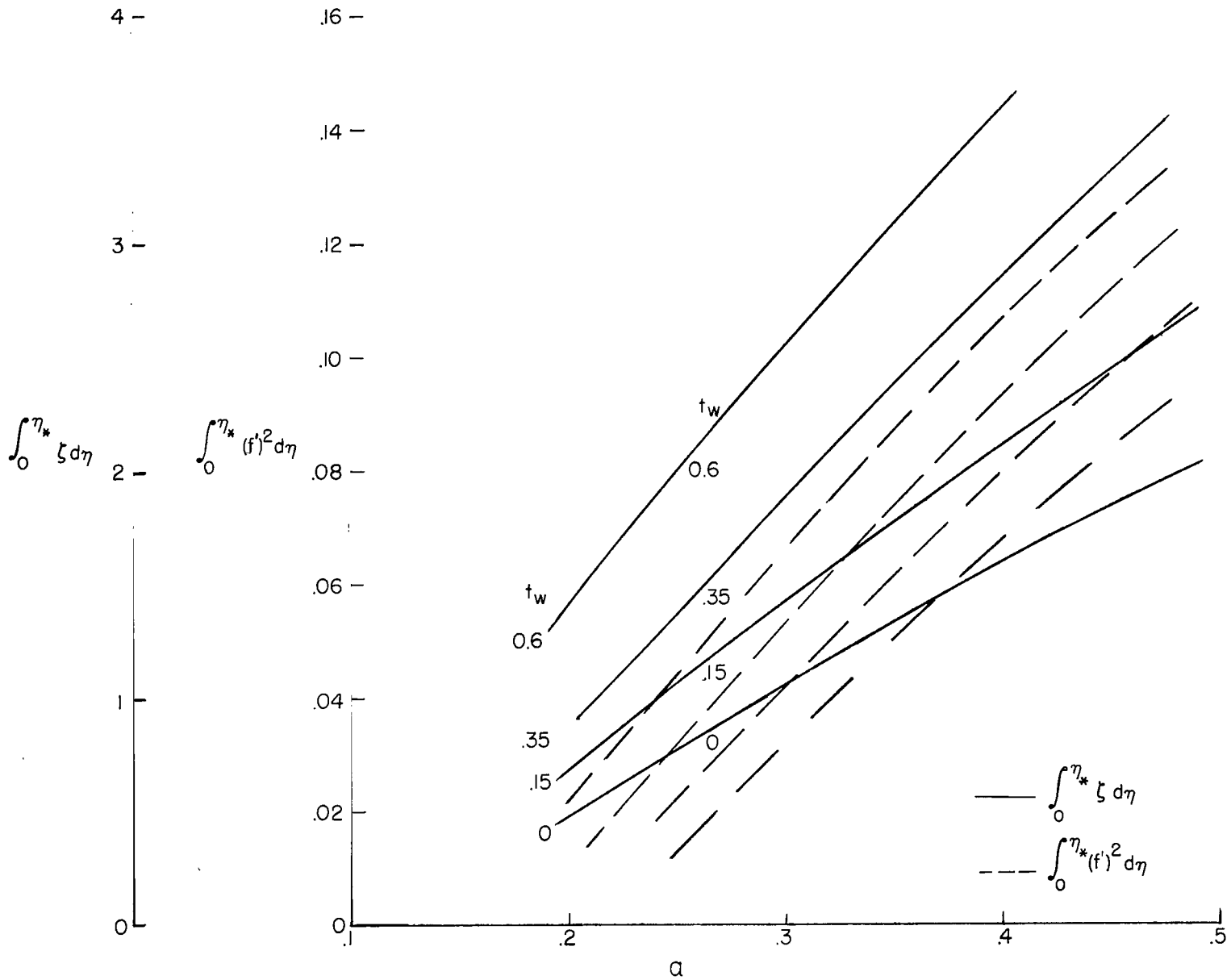

Figure 11.- Integrals of ζ and $(f')^2$ as functions of the parameter a for separated-flow profiles.